December 2020

Utilization of Kirigami Skins as a Method of Creating Bespoke Soft Pneumatic Actuators

Steven Michael Iannucci
Clemson University, stevennucc@gmail.com

Utilization of Kirigami Skins as a Method of Creating Bespoke Soft Pneumatic Actuators

---

A Thesis
Presented to
the Graduate School of
Clemson University

In Partial Fulfillment
of the Requirements for the Degree
Master of Science
Mechanical Engineering

---

by
Steven Michael Iannucci
December 2020

Accepted by:
Dr. Suyi Li, Committee Chair
Dr. Huijuan Zhao
Dr. Ian Walker

Abstract

Soft pneumatic actuators have many applications in robotics and adaptive structures. Traditionally, these actuators have been constructed by wrapping layers of reinforcing helical fibers around an elastomeric tube. This approach is versatile and robust, but it suffers from a critical disadvantage: cumbersome fabrication procedures. Wrapping long helical filaments around a cylindrical tube requires expensive equipment or excessive manual labor.

To address this issue, we propose a new approach towards designing and constructing pneumatic actuators by exploiting the principle of kirigami, the ancient art of paper cutting. More specifically, we use "kirigami skins"—plastic sleeves with carefully arranged slit cuts—to replace the reinforcing helical fibers.

This paper presents an initial investigation on a set of linear extension actuators featuring kirigami skins with a uniform array of cross-shaped, orthogonal cuts. When under internal pressurization, the rectangular-shaped facets defined by these cuts can rotate and induce the desired extension motion. Through extensive experiments, we analyze the elastic and plastic deformations of these kirigami skins alone under tension. The results show strongly nonlinear behaviors involving both in-plane facet rotation and out-of-plane buckling. Such a deformation pattern offers valuable insights into the actuator's performance under pressure. Moreover, both the deformation characteristics and actuation performance are "programmable" by tailoring the cut geometry. A computational model was developed to predict the deformation pattern of the kirigami skins. This study lays down the foundation for constructing more capable Kirigami-skinned soft actuators that can achieve sophisticated motions. Additional design variables were implemented into the kirigami patterns to generate for rectangular and rhomboid elements. A kirigami skin defined by these parameters can produce a wide range of actuation patterns.

Acknowledgments

I would like to acknowledge my committee, Dr. Suyi Li (Committee Chair), Dr. Huijuan Zhao, and Dr. Ian Walker for their assistance and support. I want to thank Dr. Li for his patience and support throughout the entire research process. In addition, I would like to acknowledge the countless number of people who lent their support and offered their insight, especially Bailey Basso and Nathan Brown from the Clemson's mechanical engineering department.

Table of Contents

List of Figures

Chapter 1

Introduction

1.1 State of Soft Actuators

The ongoing evolution of robotics toward soft, human-friendly mechanisms is natural. As the tasks of the worker have become more integrated with robotic mechanisms, there is a need for compliant and collaborative systems that improve safety over traditional *hard* robots [1]. Soft robots provide complex motion with simple construction from flexible materials. The development of new technologies and materials has pushed the exploration of the soft robotic design space [2]. Many traditional hard robots are made to mimic the structured movement of a bony skeleton, soft robots derive their design primarily from nature. Bio-mimetic inspiration is the motivation for *soft* robot's form and functionality. One of the first soft robots was a gripper, modeled after the design of the starfish [3]. On a larger scale, there have been numerous attempts to replicate a octopus tentacle: the ideal soft robot being a supple arm that can maneuver freely to any point. Researchers have attempted to imitate an octopus arm using each of the three main methods of soft actuation: variable length tendons, electro-active polymer (EAP), and fluidic elastomeric actuation (FEA). Variable length tendon inspiration is drawn from the connective tissue within typical bony structures, but has been utilized as an effective method for motion generation in several scales. Initially, a conically designed prototype utilizes cables that are actuated by an external servomotor to grip, bend, and crawl [4]. Working like tendons in the hand, Calisti et al. was able to successfully mimic an octopus's motion, yet the system is limited by the speed and power of the motors. On a smaller scale, Seok et. al showed how nickel titanium (NiTi) spring coils implemented in a meshed

appendage can be used to simulate artificial muscle fibers [5]. The mesh worm was able to crawl and steer with the peristaltic actuation of the shape morphing alloy (SMA), NiTi. Coiling the SMA wires is an effective technique to generate large deformations at slow actuation speed. Similarly, EAPs are bio-compatible materials that deform when in the presence of an electrical field and are categorized as either electronic or ionic. Electronic EAPs require high voltage fields and actuate in a matter of milliseconds, while ionic EAPs require a low voltage. The lower voltage is safe, efficient, and scalable. Ion-exchange polymer-metal composites (IPMC) have been implemented as both actuators and sensors as they bend in the presence of an electric field and also produce an electric field when deformed [6, 7, 8].

Fluidic actuators work by inflating channels or pockets to deform an elastomeric container. Inflation can be supplied hydraulically, providing large forces and has the advantage of being applied underwater [2]. A fish-inspired soft body uses hydraulic pressure to harmonically bend the caudal fin to create movement [9]. More commonly, pneumatic actuation of fluidic actuators have been explored for their possible applications as air is more abundant than oil. PnueNets, short for pneumatic networks, are a class of elastomeric actuators that are made of a collection of small, inflatable pockets. In some, each pocket can be pressurized individually, creating tailorable motion without changing the construction of the actuator. The internal design of each chamber within the actuator can be altered to inflate a particular way, as the areas with the most compliant material will be affected first. This leads to the successful creation of PneuNet robots that bend[10], grip[11, 12], and crawl [13, 14, 15]. In these systems, the pockets inflate simultaneously generating a bending as the elastomeric pockets are inextensible on the bending direction. PnueNets can be altered to complete various different tasks, but the complexity of the designs and materials does not allow for mass implementation of the technology. McKibben actuators are an industry standard of a different class of soft actuator known as pneumatic artificial muscles. They consist of a soft inflatable bladder enclosed in a mesh of inextensible fibers. Mimicking the function of a muscle, McKibben actuators shrink in length when pressurized, are longest in their relaxed state, and can achieve a strain of about 35% [16, 17]. These actuators are expensive to buy commercially as well as reproduce by oneself due to the complex construction of the outer mesh, requiring expensive materials and equipment.

Fiber-wrapped actuators have been explored as a form that could be tailored to fit numerous tasks. Each actuator consists of a two elastomeric layers with in-extensible fiber wrapped between and an internal cavity, can be tailored to a specific task. In an elastomeric tube without structural

2

constraint of the fiber an increase in pressure would cause deformations in the length and radial direction. As outlined by Connolly et al., the angle at which the fiber is wrapped can alter the deformation when pressurized by limiting the radial displacement [18]. Linear extension can be achieved by having 0° tilt on the helical, symmetric fiber-wrapping for the whole length. Bending motion is caused by the asymmetric application of inextensive material to the actuators [19, 20, 21]. Adding a off-axis tilt to the helical fibers can induce a coiling motion which is a combination of linear extension, twisting, and bending [22, 23, 24, 25]. These actuators have been able to achieve complex motion over iterations of improving prototypes.

There are issues that come with any new technology, especially within soft robotics. Currently, the manufacturing process for fiber wrapped actuators is expensive and time-consuming. The process can take multiple days due to having to wait for the elastomeric material to cure. In addition, the molds for each step of the manufacturing process must be designed and 3D printed. Unfortunately, additive printers that have a small enough tolerance with a watertight material are too expensive for most commercial users. Since each actuator is made by hand, there are additional uncertainties which cause each actuator to behave slightly differently[22, 23]. The fibers are wrapped by hand which is imprecise as the tension of the fiber is not constant from actuator to actuator, leading to non-uniform bulging at the weakest points. Fiber wrapped actuators are an option to achieve numerous functions and motions, but the lack of precision of the actuators means the high entry cost of manufacturing may not be worth it.

1.2   Introduction to Kirigami

To address the current weaknesses of soft pneumatic actuators, we propose adapting 'kirigami skins' as a method to obtain tailor-able performance of an actuator while reducing manufacturing

Linear	Triangular	Circular	Trapezoidal
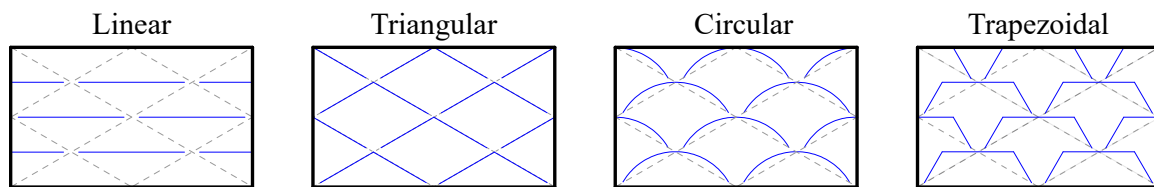
Figure 1.1: Cut shapes considered in study comparing the friction generate during strain. All four patterns are founded from the same underlying geometry, denoted by the dashed lines. The solid blue lines represent cuts made into material.

time and cost. Kirigami, originally an ancient art of paper cutting, has become popular research subject as cutting the paper increases the degrees of freedom of a sheet, giving way to unexplored applications. Carefully designing the cuts allows a thin sheet to become a sophisticated 3D shape when stretched, folded, or from other manipulation techniques [26].

The implementation of kirigami has been successful in a variety of ways. A team was able to linearly cut flexible solar cells in order to maximize their efficiency throughout the day. This specific pattern deforms out of plane when strained, as the material in between cuts becomes angled in the direction of the strain. When calibrated correctly, the cells will actuate to follow the sun the sky, generating the most energy possible [27, 28]. An advantage kirigami presents is due to the scalability of the cutting, which allows for its principles to be effective in many engineering applications. For example, cutting a collapsed honeycomb pattern into a single atom graphene sheet creates a more resilient materials by adding bistability to the sheet. When stretched too far, the skin buckles to its elongated state, releasing the force pulling the material to its original length[29]. Also, it has been demonstrated that the pattern cut into graphene sheets can be tailored to a desired stiffness [30, 31]. This principle is utilized when designing graphene as a transistor where deformation is actuated by an electronic signal [32]. On a micro-scale, kirigami patterns cut into shape memory alloys (SMAs) deform to generate motion while sensors that measure the displacement are formed from the same kirigami SMAs [33]. In addition to applications in nano and micro technology, kirigami principles have been employed in composite materials. For example, polystyrene that shrinks when under increased heat is used to create out of plane deformations of previously flat sheets [34]. It has been shown that the strategic placement of cuts into composite laminate can create previously achievable shapes by altering the fiber orientation between layers [35]. From single-atoms to complex sensors, kirigami has the potential to be effective in a broad range of applications.

Kirigami can be applied as the method of actuation or sensing in small scale mechanisms, and has been able to be effective on-board robotic systems. A crawling robot was designed with a kirigami skin that was wrapped around an internal soft pneumatic actuator. Four different patterns were tested out for their ability to generate friction by digging into the substrate as it undulated forward. The internal pneumatic linear actuator causes the skin to strain, inducing the out-of-plane deformation of the cut pattern. It was found that a trapezoidal pattern was most effective at generating the necessary friction force [36]. Critically, the skins were most efficient when plastically deformed before use, as this caused the individual trapezoids to remain slightly out-of-plane even

4

when the overall actuator is at its original length. The same cutting pattern was used on a soft-pneumatic actuator to mimic to the digging of an earthworm [37]. The addition of specifically designed cuts into the existing kirigami pattern was found to be useful as a method to adding curvature to formerly linear systems. A soft pneumatic robot was wrapped in a kirigami skin such that it slithered like a snake, mimicking the lateral movement by using the kirigami skin to act as scales and propel the robot forward [38]. All the patterns demonstrated here are simple and non-auxetic, demonstrating the broad application of the most basic kirigami.

Certain kirigami cutting patterns cause the sheet to be auxetic. By definition, having a negative Poisson's ratio is a unique trait that has been investigated for its possible applications. The simplest auxetic design is a pattern of orthogonal cuts, leaving an array of squares behind, each connected by hinges in the corners. When the sheet is placed under tension, the squares will rotate *away* from each other, growing the skin in the both the direction being pulled but in the orthogonal direction. Due to the simplicity and effectiveness, orthogonal cut kirigami is used on the linear actuators presented in this paper.

1.2.1   Kirigami Mechanics

To begin, a mathematical model describing the motion of an auxetic skin was explored. Orthogonal cut kirigami can be theoretically represented as a system of rotating squares that are connected via hinges in each corner. As the kirigami skin is an array of repeated segments, the model only needs to examine an individual element: there are periodic boundary conditions on each side of an element. The dimensions of each individual unit cell is defined in equation 1.1, where l is the length of an individual square and θ represents the angle at the connection of two squares [39].

$$X_1 = X_2 = 2l \left[\cos\left(\frac{\theta}{2}\right) + \sin\left(\frac{\theta}{2}\right) \right] \tag{1.1}$$

The size of an element based on equation 1.1 is directly related only to the opening angle. Also, due to the geometry of the system of rigid squares, the system is symmetric in both the O_{x_1} and O_{x_2} directions. Thus, as the system is extended in one direction, the same extension is seen in the perpendicular direction. Grima et al [39], outline the steps in which they mathematically prove that this structure has a Poisson's ratio of -1, for any loading direction as The Poisson's ratio is defined as the ratio of the incrementally small strain in one direction compared to the other.
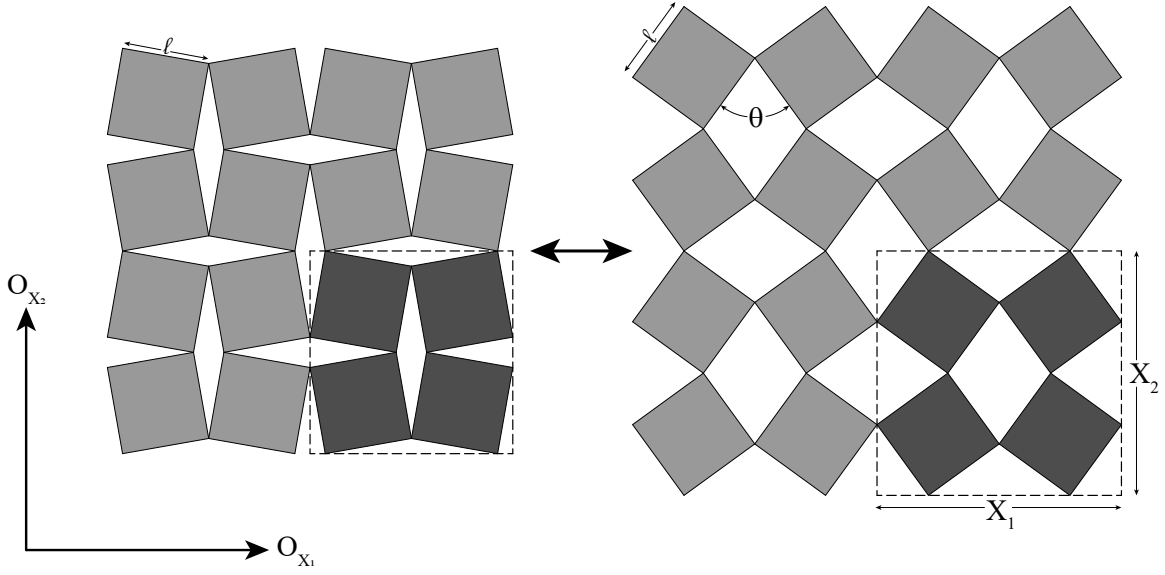
Figure 1.2: The geometry of the auxetic "rotating squares" structure. The increase of the opening angle, θ, is connected to an increase in displacement.

Auxetic systems introduce an increased stiffness to the material. In order to calculate the effective Young's modulus of the structure, it is assumed the hinges provide the stiffness to the system: defined as stiffness constant K_h. First, the strain energy, U, is defined as a function of the incrementally small strain, $d\varepsilon_i$, is shown in equation 1.2.

$$U = \frac{1}{2}E_i(d\varepsilon_i)^2 \tag{1.2}$$

Next, the work done during the rotation of the square is related to the incrementally small change in angle, denoted by $d\theta$.

$$W = N\left[\frac{1}{2}K_h(d\theta)^2\right] \tag{1.3}$$

Through the principle of conservation of energy, the strain energy is the ratio of work over the *volume* in which work was done on. For a planar system, the volume is product of the overall dimensions of the element, X_1 and X_2. By equating the work (eq. 1.3) and strain energy (eq. 1.2) and solving

6

for the Young's modulus, E_i, equation 1.4 is derived.

$$E_1 = E_2 = K_h \frac{8}{l^2} \frac{1}{1 - \sin(\theta)} \tag{1.4}$$

Since the structure is perfectly auxetic, the modulus of elasticity is the same in both planar directions. The strength is dependent on the stiffness of the hinges, but it is determined by the side length of an individual square.

The Effective Young's modulus is vital when modeling the system, as it is necessary when relating the force applied to the induced strain through Hooke's law, $\sigma = E\varepsilon$. Similar patterns, like a system of rotating triangles or system of rotating parallelograms, have been investigated for their theoretical auxetic deformation behavior [39, 40, 41]. Even though the inspiration for orthogonal cut kirigami is purely theoretical, the principles laid out hold true, especially at small strains. Rafasanjani et al. took it a step further in Buckling Induced Kirigami [42], where the principles learned from simple rotating squares are applied to orthogonal cut sheets. A cutting pattern is proposed with hinges of length δ that connect squares of length l. Again, the mechanics of the entire system can be simplified down to single unit cell that is under a uniaxial force that generates a stress, $\sigma_x = f/(2lt)$, where t is the thickness of the sheet. The applied force generates a moment in the hinges, found as equation 1.5, which is equated with the couple being induced by the internal load of deformation of the hinges.

$$M = \frac{1}{4}\sigma_x l^2 t = \frac{EI_i}{\rho_i} \tag{1.5}$$

The curvature of the hinge is approximated as $\rho_i \approx \frac{\delta}{2\theta_i}$, and the in-plane moment of inertia of the hinge is $I_i = \delta^3 t/12$ as the hinge will be bending about the z-axis. The assumption of small angle deformation $(\cos(\theta_i) \approx 1, \sin(\theta_i) \approx \theta_i)$ is used to further simplify as the strain can then be approximated as a function of the opening angle. The previous equations are combined, the applied stress is solved for, and are then simplified to equation 1.6.

$$\sigma_x = \frac{2}{3}E\left(\frac{\delta}{l}\right)^2 \varepsilon_x \tag{1.6}$$

The stress - as a function of the induced strain - displays how the hinge size and element length directly alter the stiffness of the sheet. Equation 1.4 for a theoretical sheet includes the same

7

relationship as equation 1.6, as the hinge size is represented by the hinge stiffness K_h.

Grima et al. and Rafsanjani et al. analyzed the underlying mechanics of the orthogonal cut kirigami. It is outlined that in the presence of a uniaxial force, the sheet will initially undergo a stage of linear elastic response. The cuts in the sheets will slightly open and in-plane deformation will occur at the hinges. The stiffness of the sheet is related to the dimensions of the kirigami design dimensions. The kirigami will be defined by the previous equations until the hinges buckle out-of-plane.

1.3   Research Overview and Objective

Soft robotics will continue to be involved in a variety of different applications as the materials and technology become more advanced. The current state of actuation methods are useful and effective at the individual tasks that they are designed for, especially as they can withstand increasingly larger loads. These bespoke robotics are expensive to purchase or construct as they require expensive raw material or intense manufacturing process. We propose the basic application of auxetic kirigami on soft actuators to create a programmable performance. The stiffness of the kirigami sheet can be altered so that the actuator has a desired stroke or pressure range.

In the following sections, a parametric kirigami skin is proposed as a method to control the actuation of soft linear pneumatic actuators. Kirigami has not been used for ability to affect the deformation of soft actuators in this manner before. Auxetic kirigami principles have been explored for their novelty, but the application on board mechanical systems is still unknown. We outline the novel manner that varying the two design variables causes the skin's performance to vary during actuation and uniaxial tension. It will be demonstrated that the hinge size affects the maximum deformation of a skin. In addition, the number of elements cut into a skin can affect the amount of internal pressure the skin can withstand. Overall, with only two design variables, it is possible to create a kirigami wrapped soft pneumatic actuator with bespoke stroke pattern.

The unique deformation pattern of the cylindrically wrapped skin is defined into three distinct phases during uniaxial testing and actuation. During each phase, the skin responds differently to increased pressurization. Also, we explore the hysteresis due to plastic deformation of the skin that occurs at the hinges.

A mathematical model was created to simulate the deformation pattern of the skins. The

model was able to accurately portray the displacement of the skin during uniaxial testing. In addition, a third design parameter was explored as a way to maximize the stroke of the actuators. By altering the *height* of each rotating segment, a mesh of rotating rectangles is created. As the rectangles becomes skinnier, the greater the maximum stroke can be achieved, giving way to more possible stroke patterns. Lastly, a kirigami pattern was designed to generate the twisting motion of the soft actuators when inflated. By adding an angular offset to the typical orthogonal cutting pattern, each element was now a set of rotating parallelograms. The offset angle creates a skin with an uneven forces, causing a twisting motion to occur during out-of-plane deformation.

Although kirigami skins have been utilized on soft pneumatic actuators, this research proves that they can be an effective way to create tailor-able stroke performance. Recently, other research has been presented on how to embed kirigami skins within the walls of soft elastomeric actuators to create bespoke inflation patterns. Our research shows that it is possible to apply simple, fast, and cheap kirigami skins to soft actuators. The actuators presented demonstrate that utilizing kirigami in this unique matter is feasible. The steps to create a model which matches the skin performance has been started to allow for rapid prototyping to fit an individual's needs.

Chapter 2

Orthogonal Kirigami

2.1 Design

Outlined in the introduction, we are proposing a actuation system in which a kirigami skin can be applied to a desired performance. The skins presented are based off of the auxetic orthogonal cutting pattern discussed previously. The simplicity of the cutting design allows for easy creation of a variety of deformation responses of the skin by only altering two design variables. This allows for the easy transition if an actuator needs to be repurposed for a new stroke performance. The overall dimensions of the skin are kept uniform in order for all the actuators to be the same during testing.

2.1.1 Design Of The Kirigami Skin

The kirigami skins in this study have periodically distributed and mutually orthogonal cuts that divide the sheet into an array of repeating elements (Figure 2.1). Each element can be described by a few design parameters, including the element size L, slit cut length l_c within the element, and the "hinge" size δ between the cuts. In this study, we fix the total length C of the kirigami skin because it is supposed to wrap around a cylindrical fitting of 50.8mm diameter (aka. $C = \pi d_0 = 159.6$mm). So the element size L is related to the total number of elements N along the length of kirigami skin according to Equation 2.1. The total height of a kirigami skin is set at 127.0mm.

$$L = \frac{C}{N} = 2\delta + l_c.$$
(2.1)

Besides the number of elements N along the skin length, we define another independent
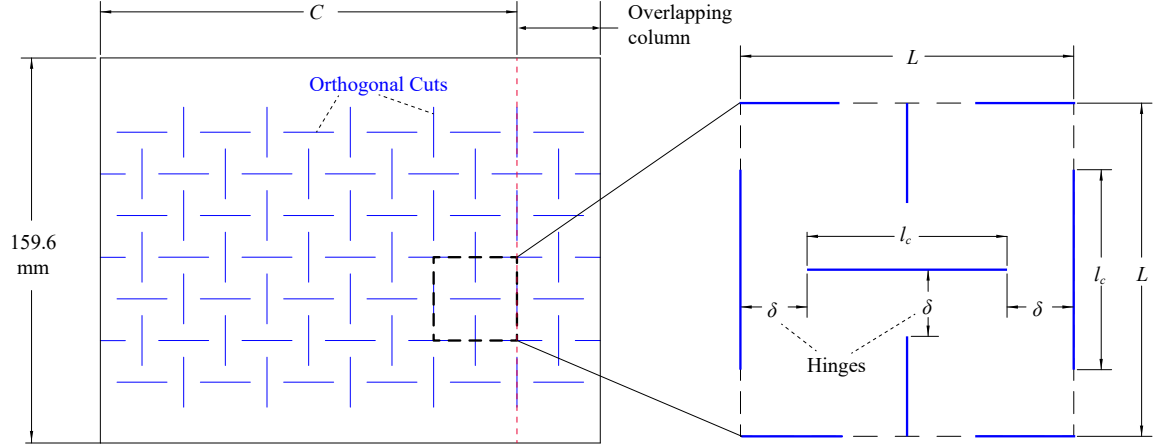
Figure 2.1: An example of kirigami skin design: Here, a single element is scaled up to show the geometry of the cuts (shown by solid blue lines) made in the sheet material. The hinges between cuts are shown as δ. The column of elements to the right of the red dashed line is for overlapping during assembly.

design variable R as the ratio of the slit cut length over hinge size in that

$$R = \frac{l_c}{2\delta}. \tag{2.2}$$

As R increases, the cut becomes relatively longer, leaving smaller hinges to connect the square facets. To ensure reliable actuation performance, we add an extra column of elements and overlap this column to the one on the other side of the kirigami skin when we wrap it around the interior balloon. Without this overlapping, the kirigami skin would have a discontinuous break, causing the inner tube to bulge through under pressure.

2.1.2   Design of Soft Linear Actuator

We use 50mm diameter balloons (Qualatex, North Wichita, KS) to contains the pneumatic pressure. Each balloon, with an initial length of about 40mm, is connected to 3D-printed end caps and inflated to the length of the undeformed kirigami skin before testing. The kirigami skin is attached to the end caps using double-sided tack film and wrapped around the caps and interior balloon. Again, we secure an overlapping column of elements using a double-sided tack film and then wrap vinyl tape outside of the skin-end cap assembly for extra support (Figure 2.2).

To measure the free stroke of these actuators, we mount one of the actuator end caps

11
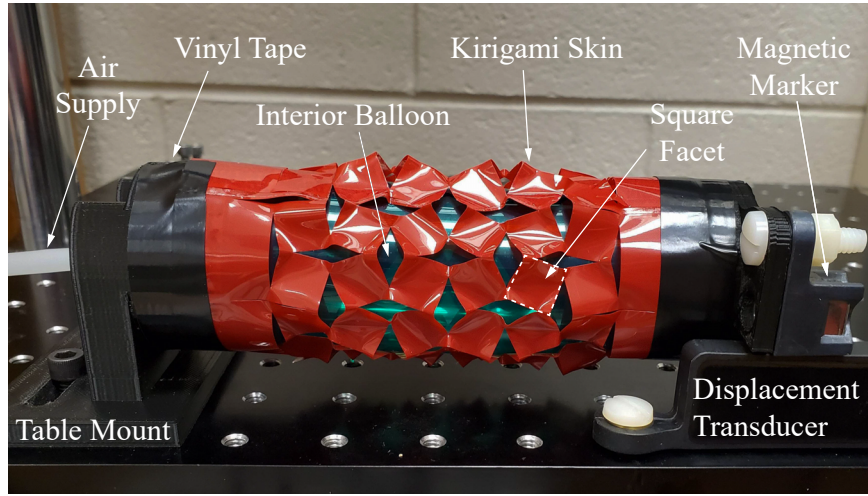
Figure 2.2: A kirigami-skinned soft pneumatic actuator under internal pressure, showing the linear extension motion.

to a non-ferrous bed while leaving the other end cap free. A non-contact electromagnetic linear displacement transducer (SPS-L075-HALS, Honeywell, Charlotte, NC) was mounted to the bed, with the magnetic positional marker secured to the free-moving end cap (Figure 2.2). During pressurization, the magnet will rest on top or hover above the displacement transducer allowing for what is assumed to be frictionless measurement of the end cap location.

Pneumatic pressure is supplied using a solenoid valve (ControlAir 900X, Amherst, NH) and measured by a gauge pressure sensor (SSCDANN005PGAA5, Honeywell, Charlotte, NC). Once the actuator reaches full extension, we release the pressure by a manual relief push-button valve, which returns the actuator to its initial length. The pressure sensor and displacement transducer readings are linked using LabView via an analog data acquisition instrument (National Instruments, Austin, TX).

In what follows, we show how that the kirigami skins can effectively constrain an inflatable balloon and transform its volumetric expansion into extension, and how adjusting the two independent design parameters (aka. element number N and cut ratio R) can create a broad spectrum of skin deformation pattern and actuator performance.

2.2 Parametric Study

2.2.1 Methods
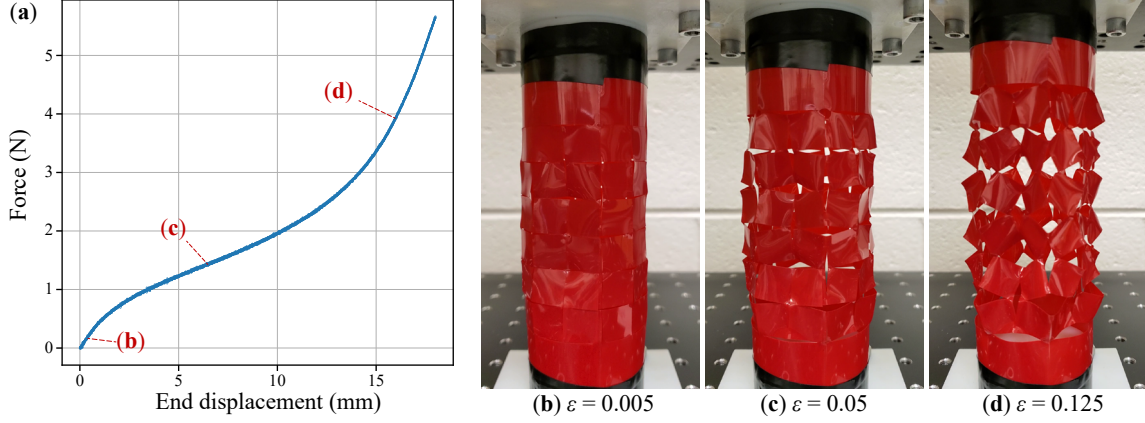
Figure 2.3: Deformation pattern of a sample Kirigami skin with $N = 6$ and $R = 6$. a): The force-displacement curve, notice that only the extension responses are shown here. The three different phases of deformation are highlighted at $\varepsilon = 0.005, 0.05, 0.125$. (b, c, and d): The external shapes of the skin at the noted strain levels.

We first analyze the deformation characteristics of the kirigami skin *alone* by uniaxial tensile testing, because the kirigami deformation under this loading condition is directly related to the actuation performance. We first use an FCX4000 plotter (Graphtec, Tokyo, Japan) to cut an array of perpendicular slits in a 0.5mm thin Artus Plastic Shim Stock. These kirigami skins are connected to two 3D printed fittings via double-sided tape, and each fitting has a diameter of 50.8 mm and a height of 25.4 mm. The overlapping column of kirigami elements is also secured with thin, double-sided tape to create a cylindrical-shaped skin with a uniform cut pattern. Also, vinyl tapes are wrapped around the exterior of the skin and mount to ensure fixed end conditions. Finally, we secure the assembly to an eXpert 5061 universal tester machine with an 25 lb load cell (ADMET, Norwood MA, Figure 2.3).

For the tensile tests, we first stretch the kirigami skin samples to an initial deformation at a rate of 0.5 mm/s and then cycle back to the starting position. After completing three initial stretching cycles, we increase the tensile deformation by 2 mm in every subsequent stretch.

We fabricated and tested 24 kirigami skin samples with unique cutting pattern designs. The samples have ($N =$) 6, 8, 10, or 12 elements in the circumferential direction (or length direction of

the unwrapped flat Kirigami sheet). The cut ratio R defined in Equation 2.2 is varied from 2 to 7 for each N value.

2.2.2   Deformation Phases

Figure 2.3(a) displays the force-end displacement relationship of a kirigami skin ($N = 6$, $R = 6$) during extension, from which one can observe three distinct phases. At small end displacements (or small strain ε), the response of kirigami skin is relatively linear without any significant deformations (Figure 2.3(b)). As the end displacement increases to a critical threshold, kirigami skin deformation enters its second phase as its square facets began to rotate and deform out-of-plane. As a result, the slit cuts begin to open (Figure 2.3(c)). These out-of-plane deformations seem non-uniform and random initially. However, as the end displacement gradually increases, the square facets start to "snap" and align with each other, and the hinges between the facets start to buckle (shown by the small drops in the reaction force curve) until they all settle into the final deformation pattern (Figure 2.3(d)). In this final pattern, every square facet rotates oppositely to its adjacent neighbors, and the slit cuts become rhomboid-shaped gaps. Once reaching this final deformation pattern, the kirigami skin enters the third phase of deformation, where the skin deforms mainly at its hinges. It is worth noting the cylindrical kirigami skin is not as stretchable as a unwrapped flat kirigami sheet with the same cutting pattern design, because there are additional deformation compatibility constraints in the circumferential direction.

2.2.2.1   Plasticity

The plastic deformation of the hinges plays an essential role in the nonlinear response of kirigami skin. Figure 2.6 shows the force-deformation relationship of two skin samples with the same cutting pattern design ($N = 6$, $R = 6$) but different loading sequences. For the first sample, we stretch it with a 16mm end displacement for the first three loading cycles and then increase the end displacement to 18mm in the next two cycles. For the second sample, we stretch it with an 18mm end displacement in the first loading cycle, and then reduce the end displacement by 2 mm in every subsequent cycle. In different loading cycles, we observe different force-displacement curves during the stretch, as well as energy loss and hysteresis due to plastic deformation in the hinges. The force-displacement curve and hysteresis magnitudes vary significantly depending on the loading history. First, if the total end displacement does not change, the kirigami skin becomes softer and provides

14

less resistance to the extension after every loading cycle, and its hysteresis also reduces (e.g., from cycle 1 to 3, or from cycle 4 to 5 in Figure 2.6(a)). These changes are probably because the hinges become predisposed (or preconditioned) to the out-of-place buckling. However, if we stretch the kirigami skin with a new end displacement that it has never experienced before (e.g., from cycle 3 to 4 in Figure 2.6(a)), we can observe a jump in resistance and hysteresis. Secondly, if we stretch the kirigami skin with a maximum end displacement without failure (e.g., cycle 1 in 2.6(b)), the skin shows a consistent force-displacement curve *during extension* in the subsequent loading cycles that have smaller end displacements (e.g., cycle 2 to 5 in 2.6(b)). Such consistency in the nonlinear responses comes from the fact that the hinges in the kirigami sheet have been plastically deformed as much as possible without failure, so no new plastic deformation can occur in the following load cycles.

2.2.2.2 Parametric Analyses

Finally, we observe that the two independent kirigami design parameters (N, R) have a strong influence on the overall nonlinear responses. The cut ratio of R relates to the maximum strain achievable by the kirigami skin samples (Figure 2.4(a)). Our samples with the largest hinge size or shortest slit cuts ($R = 2$) can withstand much higher tensile forces, yet fail at significantly lower strains. The large hinge size in these samples prevents the slit cuts from opening significantly and causing the skin to enter the third phase of nonlinear responses at a smaller stretch. On the other hand, kirigami skins with the smallest hinge size or the longest slit cuts ($R = 6, 7$) allows for a more elongation with less reaction force. The square facets in these samples can rotate by the largest angle possible according to the kinematic constrain. Finally, the maximum stretch at failure increases significantly as R increases (Figure 2.4(c)).

The number of elements in the kirigami skin (N) relates to the magnitude of the reaction force at a given stretch. Generally speaking, skins with smaller N, or large elements size, give lower resistance force. Moreover, the element size does not seem to affect the maximum stretch at failure (Figure 2.4(b, c)).

2.2.3 Phases of Actuation

In the actuation tests, the kirigami skins show similar deformation patterns to those observed in the uniaxial tensile tests. Figure 2.5(a) displays the pressure-stroke curve of an actuator during its
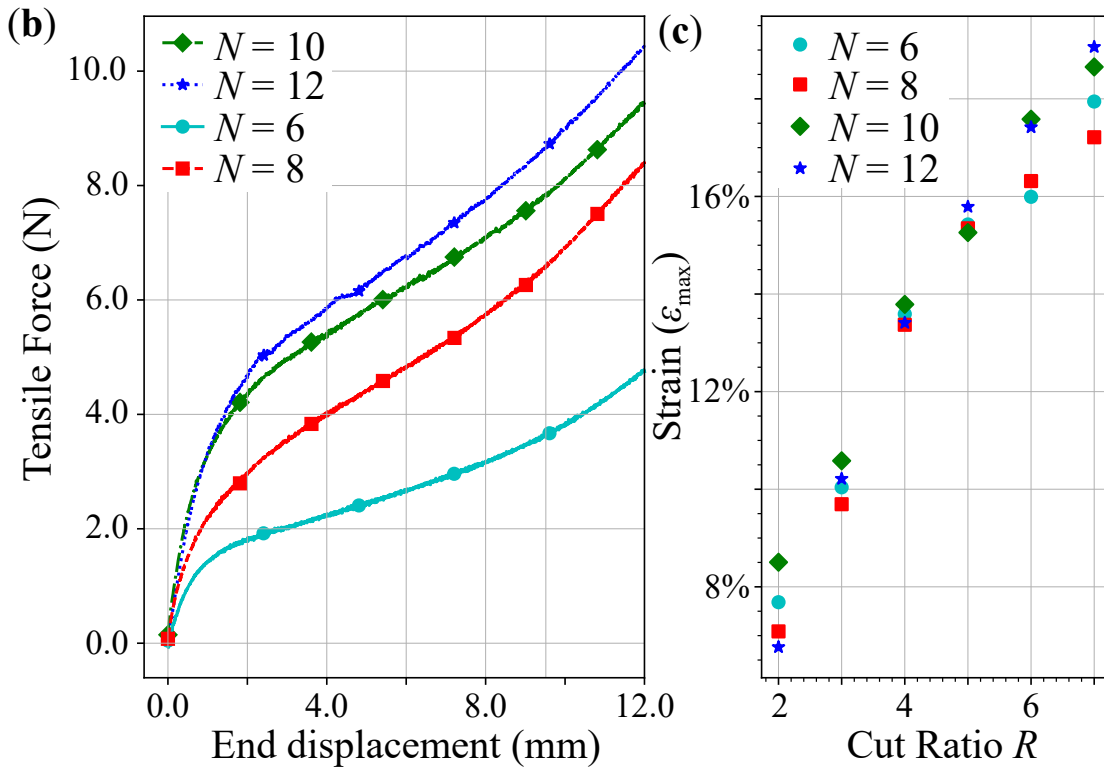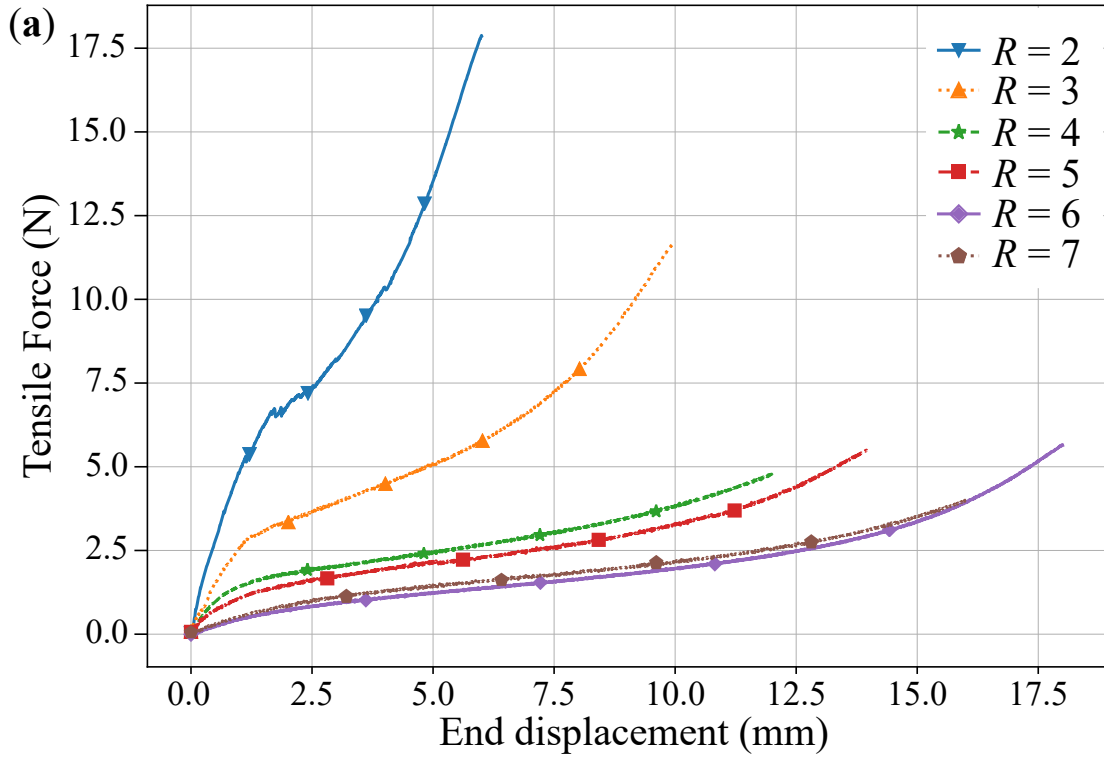
Figure 2.4 (previous page): Correlations between stretch response and cutting designs of the Kirigami skin. (a): Comparing the force-displacement curves of kirigami skin samples with the same element number $N = 6$ but different cut ratios. (b) Comparing the force-displacement curves of samples with the same cut ratio $R = 4$ but different element numbers. Again, only the stretching part of loading cycles are shown here for clarity. (c) The maximum strain of each sample at failure.

(a)

(d)

(c)

(b)

(b) $\varepsilon = 0.0025$

(c) $\varepsilon = 0.02$

(d) $\varepsilon = 0.125$
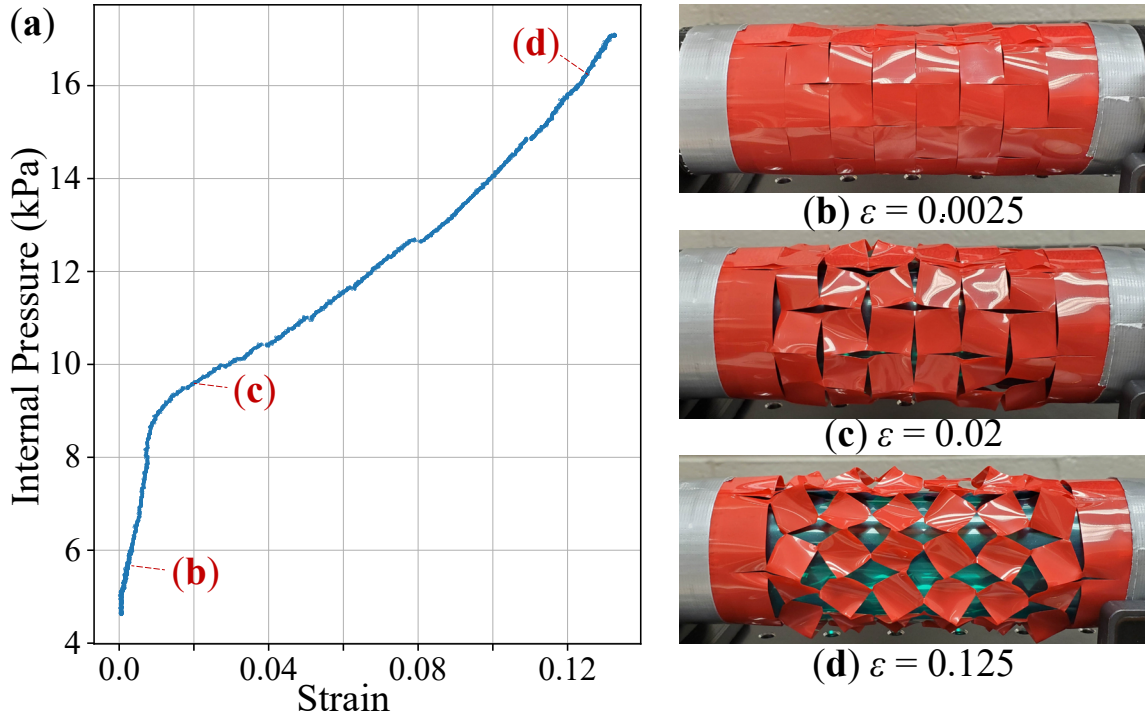
Figure 2.5: Linear extension actuator with a Kirigami skin of $N = 6$ and $R = 6$. (a): The pressure-stroke relationship of this actuator. Notice that only the pressuring phase is shown here for clarity. The different phases of deformation are highlighted at $\varepsilon = 0.0025$, 0.02, and 0.125. (b, c, and d) The actuator deformation at these strain levels.

pressurization phase. Initially, the kirigami skin shows minimal deformation at low pressure (Figure 2.5(b)), and this stage directly relates to the first phase of the skin stretch tests shown in Figure 2.3. Once the pressure reaches a critical value, the square facets in the kirigami skin begin to rotate, and the hinges start to buckle out-of-plane as displayed in Figure 2.5(c). However, due to the contact force from the interior balloon, we do not observe the random "snaps" that are evident in the skin stretch tests. As the pressure continues to increase, the square facets in the kirigami skin rotate towards the maximum possible angle allowed by the kinematic constraints.

On the hand, the Kirigami skin deformation in the actuator test start to differ from the tension test as the stroke becomes high. Figure 2.5(d) shows the actuator close to its maximum stroke. At this stage, the balloon has fully expanded and filled the entire volume enclosed by the kirigami skin. It pushes the kirigami skin from inside and constrains the skin deformation. As a result, we do not observe a significant third phase, as seen in the skin stretch tests in Figure 2.3, especially when the cut ratio is relatively small.

2.2.3.1 Plasticity

The kirigami skin shows a similar plastic behavior to those observed in the skin tensile tests. That is, the response of the skin during pressurization depends on the maximum strain previously achieved by this sample. Figure 2.6(a) shows the response of an actuator sample over five pressurization cycles. In each cycle, we increase the pressure until this actuator reaches a new maximum stroke that it has not achieved before. Due to the progressively increasing plastic deformations in the hinges, the kirigami skin shows less resistance against pressure over the loading cycles, thus providing better performance in terms of the free stroke at a given pressure. Therefore, in order to create an actuator with consistent performance over many pressurization cycles, the kirigami actuator must be pressurized to its maximum strain without failure as a pre-conditioning procedure before practical implementation. Figure 2.6(b) presents the performance of an actuator sample that is pre-conditioned by a maximum free stroke of 10% (pressurization cycle 1). Once this pre-condition is complete, the actuator operates with a lower stroke and shows reliable repeatability.

2.2.3.2 Parametric Analyses

Similar to the skin stretching test, actuation performance of the kirigami actuator is closely related to the underlying cutting pattern design. For example, a larger cut ratio of R in the kirigami
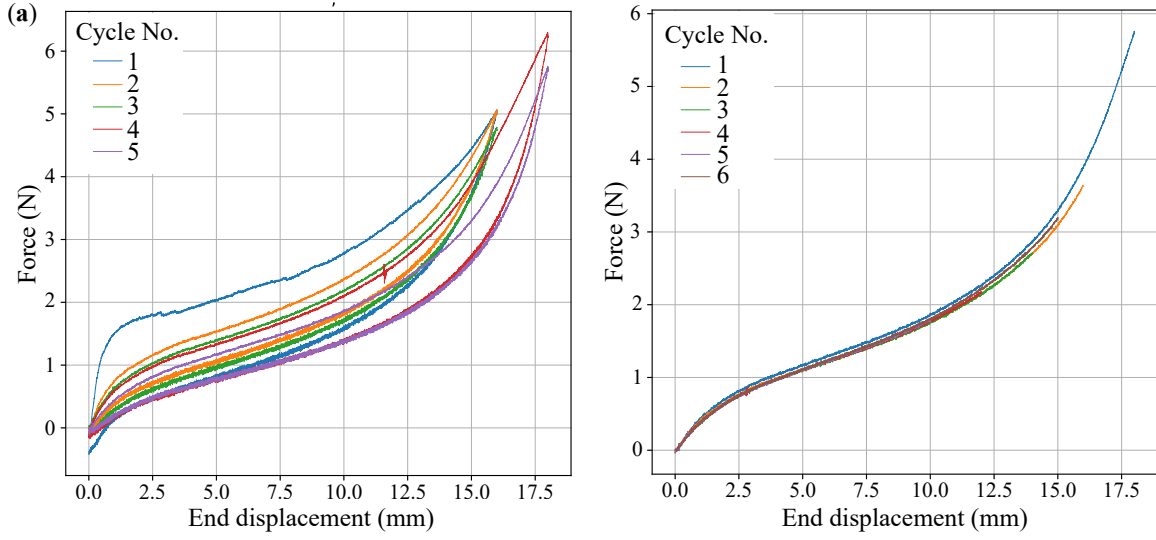
Figure 2.6: Plastic deformation of the kirigami skin under stretch. (a) The force-displacement curves of a sample, $N = 6$ and $R = 6$. Three cycles to 16 mm of displacement and two cycles of 18 mm of displacement are presented. (b) The force-displacement curves of a sample during elongation. The sample was stretched to 18 mm to start, and then stretched 2mm less in the subsequent cycles. Notice that only the stretching part of load cycles are shown here for clarity
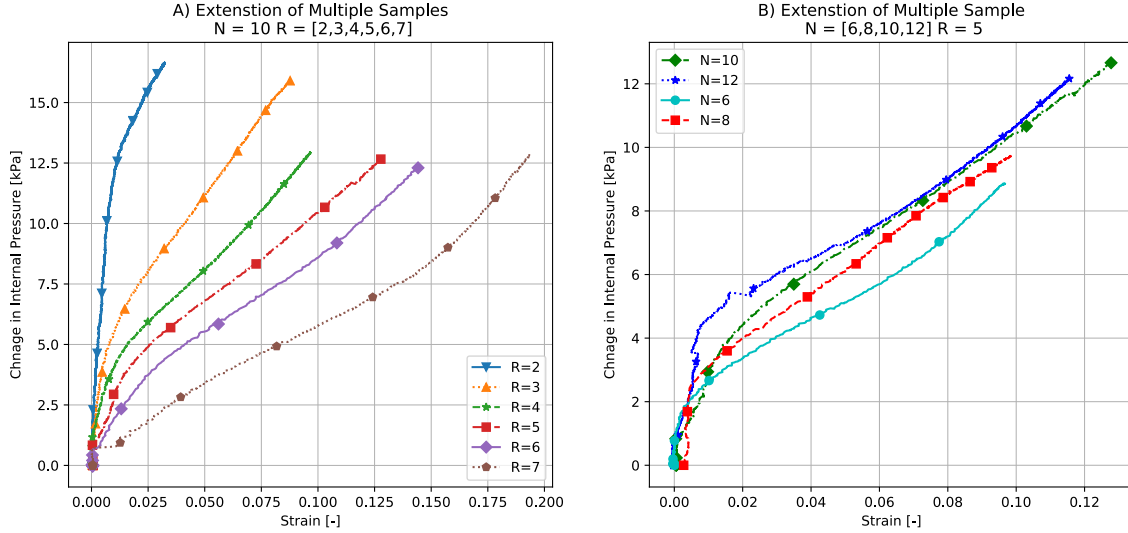
Figure 2.7: The correlations between the actuator performance and underlying Kirigami designs. (a) Comparing the pressurization response of various samples with the same element number $N = 10$ but different cut ratios. (b) Comparing the response of samples with the same cut ratio $R = 5$ but different element numbers.

19

skin gives a greater maximum free stroke (Figure 2.7(a)). This is because the smaller hinges corresponding to the high cut ratio can rotate to a greater opening angle. In our test, we are able to achieve close to 20% of free stroke with $R = 7$. On the other hand, kirigami skins with a smaller cut ratio (or large hinge size) can withstand higher internal pressure. The number of elements in the kirigami skin, on the other hand, has a limited effect on the actuation performance (Figure 2.7(b)). Generally speaking, a kirigami skin with more elements requires more pressure to reach the same free stroke.

2.2.4 Discussion

In this study, we propose and examine the concept of soft pneumatic actuators with kirigami skins defined by an array of mutually orthogonal cuts. These slit cuts allow for the skin to deform non-uniformly and convert the internal pressure into linear motion. To understand the mechanics of these cylindrical kirigami skins under tension and its correlation to pneumatic actuation performance, we first tested skin samples *alone* in uniaxial tension. The behaviors of these skin can be described as three-phase deformation cycles in response to stretching. Importantly, the second deformation phases are defined by the in-plane rotation of the square facets and out-of-plane buckling of hinges, generating a nonlinear extension curve. Then, we wrap the kirigami skins around an inflatable balloon to create linear actuators. The skins proved to be an effective mechanism to convert internal pressure into linear motion, showing a similar deformation pattern as these observed in the tensile tests.

The kirigami skin performs well as a mechanism that transforms the pressure-driven volumetric expansion into a linear actuator extension. Moreover, one can prescribe the actuation performance in terms of free stoke by fine-tuning the underlying kirigami cutting pattern design according to the specific application requirements. For reliable and repeatable actuation performance, each kirigami skin should be pre-conditioned by being stretched to its maximum length without failure before being used. Moreover, the actuator can remain pressurized sufficiently so that the skin never exits the second deformation phase, offering a nearly linear correlation between internal pressure rise and free stroke. The results of this paper pave the foundation for establishing a design and analysis framework for constructing kirigami-skinned pneumatic actuators with sophisticated actuation capability.

2.3 Modeling

2.3.1 Computation Model

A computational model was adopted from earlier work [39, 42] in order to predict kirigami skin behavior and actuator performance. Developed on open-source Python, the purpose of the model is to be a cheap and efficient tool to model, understand, and predict the behavior of the kirigami skins as a method of converting the internal pressure into linear motion of soft actuators. Currently, kirigami elements and skins have been modeled in Finite Element Software which is expensive and difficult to master [42, 43]. In addition, accurately representation of the entire kirigami actuator system is challenging as pressurized latex balloons in conjunction with the skin are complex to model. The results of the mathematical model are then compared to the experimental data of both testing methods in which the kirigami skin was implemented. The goal of the computational model is to create a quick, time and computationally, method to predict the motion of an actuator and its kirigami skin. Further work could adapt the model to find the correct dimensions of a kirigami skin when given a desired actuation pattern.

The base mathematics of this model are from Grima et al. [39] and Rafasanjani et al. [42] with slight deviations to fit our cylindrical skins with a loading direction, $\gamma = 0$. Continuing from the introduciton, the initial in-plane rotational model, explained by equations 2.3-2.5 and denoted by subscript i, are applicable due to the loading angle having negligible affect on the system. During pure in-plane rotation, the Poisson's ratio of the skin is -1, independent of the loading direction. The kirigami skins initially start in a phase of extension through the in-plane rotation of the individual square elements. The orientation of the element with respect to the axis (ϕ) defines the strain of the element, shown by equation 2.3 [39].

$$\varepsilon_x = cos(\phi) + sin(\phi) - 1 \tag{2.3}$$

The strain energy density of the elements is defined as the summation of strain density of each hinge on an element, shown in equation 2.4 [39]. For all orthogonal designs, there are 8 hinges that connect the element of interest to the rest of the system.

$$U_i = \frac{1}{2}\overline{E}\varepsilon_x^2 \tag{2.4}$$
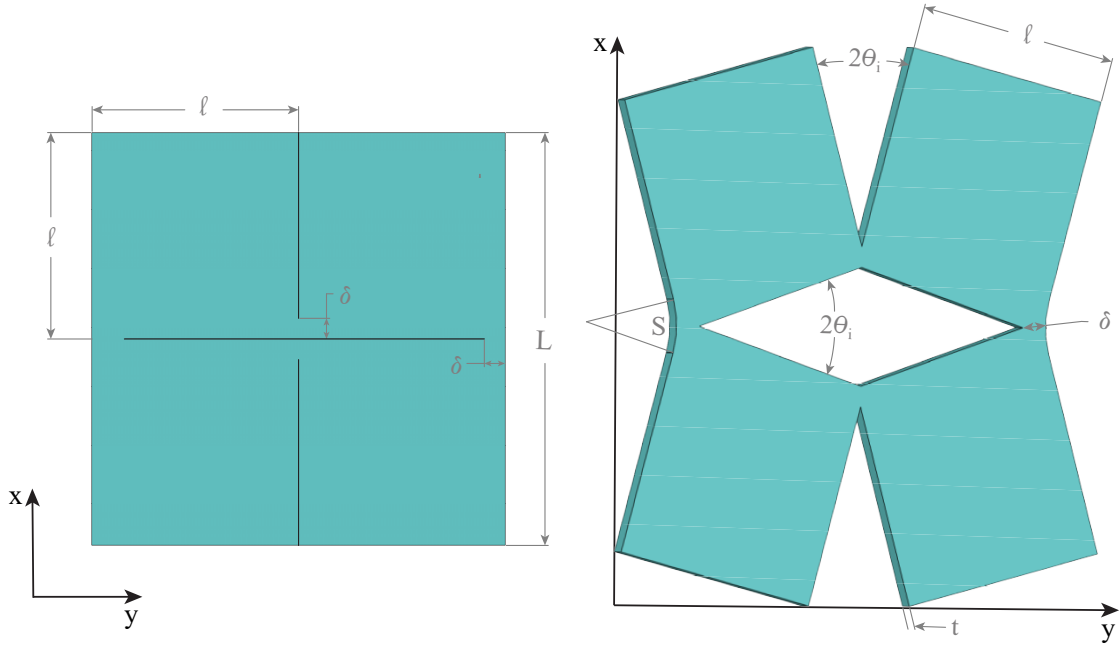
Figure 2.8: Diagram of an novel kirigami element in A) its unopened state and B) deformed state.

The effective Young's modulus of the perforated sheet, $\overline{E}$, is presented in equation 2.5, where E is the Young's modulus for the material used [42]. The effective Young's modulus is a function of of both δ and l, showing that the design parameters affect skins sensitivity to deformation in this phase. As the hinges (δ) becomes smaller, the slope of the stress-strain curve will be shallower.

$$\overline{E} = \frac{\sigma_x}{\varepsilon_x} = \frac{2}{3}E\left(\frac{\delta}{l}\right)^2 \tag{2.5}$$

The in-plane model defines the first phase of deformation, while the buckled model represents the second phases of expansion through rotation of buckled hinges. Rafsanjani et al. outlines that the switch from one phase to another occurs st the critical strain[42]. The critical strain is defined as the strain where the hinges being to buckle, equation 2.6 [42] . The critical strain is not function of hinge size, only the overall size of each element. As the number of elements (N) increases the skin will buckle at higher strains.

$$\varepsilon_c = \frac{1}{2}\left(\frac{t}{l}\right)^2 \tag{2.6}$$

22

At this point, the strain energy of the element that has buckled out of plane, U_o, is less than if through pure in-plane rotation. The overall strain energy for buckled element is defined in equation 2.7 [42].

$$U_b(\varepsilon_x) = U_i(\varepsilon_c) + U_o(\varepsilon_x) \tag{2.7}$$

The strain energy density of the out-of-plane elements is defined in equation 2.8 [42]. Until this point, the mathematics outlined have been previously been explained. In order to accurately represent the kirigami skins, some of the equations outlined in *Buckling Induced Kirigami*[42] were not an accurate representation of kirigami with a loading direction of 0°. The difference in loading direction affects all aspects of the out-of-plane deformation process, from the how the hinges buckle to the magnitude of each opening angle. Again, the strain energy for all 8 hinges was accounted for, while $I_o = \frac{\delta^2 t^2}{12}$ was used for the moment of inertia of the buckled hinges to account for bending about the axis parallel to the hinge. The inner radius of each out-of-plane hinge is defined as $\rho_o = \frac{\delta}{2\theta_{oj}}$, and volume is $V = 4l^2 t$. θ_{oj} represents the two possible opening angles of the buckled elements. The out-of-plane strain energy density is expressed in equation 2.9.

$$U_o = 4 * \frac{1}{2V} \int_o^\delta \frac{EI_o}{\rho_{o1}^2} ds + 4 * \frac{1}{2V} \int_o^\delta \frac{EI_o}{\rho_{o2}^2} ds \tag{2.8}$$

$$U_o = \frac{1}{6} E \left(\frac{\delta t}{l^2} \right) (\theta_{o1}^2 + \theta_{o2}^2) \tag{2.9}$$

Once the elements have buckled to their stable out of plane position, a pattern can be determined by the elements behavior. β is the angle between yz-plane and the edge of the element, while α is the angle between the xy-plane and element's face. Equation 2.10 shows how β is a function of the strain on the element.

$$\beta = \arcsin \left(\frac{1 + \varepsilon_x}{\sqrt{2}} \right) + \frac{\pi}{4} \tag{2.10}$$

In turn, α can be solved for in equation 2.11, where β_x represents β at any strain greater than ε_c. β_c is the angle at ε_c, and is added to ensure that $\alpha = 0$ at ε_c.

$$\cos(\alpha)^2 = 1 - \tan(\beta_x - \beta_c) \tag{2.11}$$
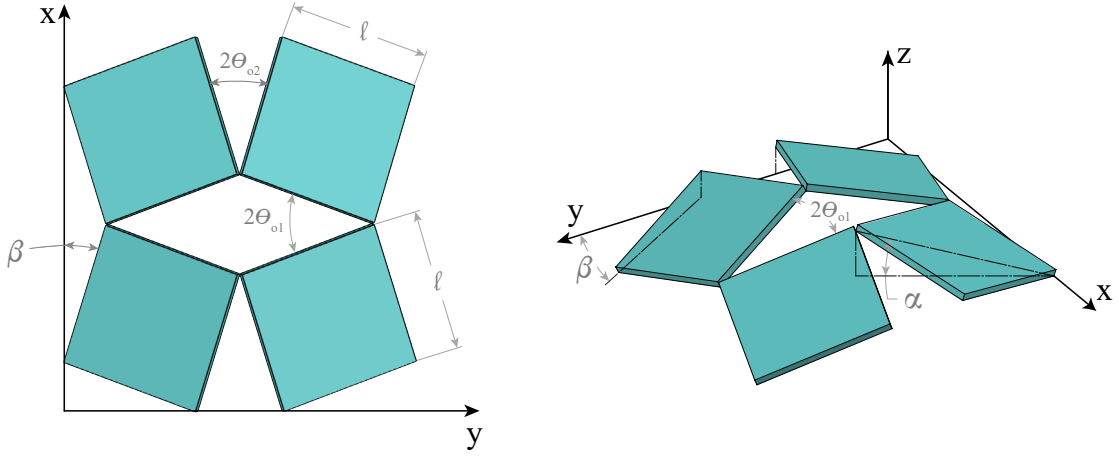
Figure 2.9: The out-of-plane model of the kirigami skin in a A) top-down view and B) Isometric View.

The opening angles are approximated as $\theta_{o1} \approx \alpha$ and $\theta_{o2} \approx \beta$. In *Buckling Induced Kirigami* [42], the opening angles are studied as a function of the loading angle. It is shown that the values for α and β are similar to those presented in the finite element results for θ_{o1} and θ_{o2} when $\gamma = 0$.

Independent of what deformation phase the skin is experiencing, the stress is found as in equation 2.12. The stress is solved for as the change in strain energy density over an infinitesimal strain $\Delta\varepsilon_x$. The force acting on the element along the x-axis ($\gamma = 0$) is solved for in equation 2.13.

$$\sigma_x = \frac{\mathrm{d}U_b}{\mathrm{d}\varepsilon_x} = \frac{U_n - U_{n-1}}{\Delta\varepsilon_x} \tag{2.12}$$

$$f = (2lt)\sigma_x \tag{2.13}$$

The Python code of the model can be found in appendix B. In order to run the script, the user sets the maximum strain, the number of iteration to run, and the design parameters of the kirigami element. In a loop, the strain energy of both in-plane and out-of-plane elements are calculated. The difference in energy from the previous iteration is divided by the strain step size. The model then decides which deformation phase the system is in and calculates the force accordingly. The code stops when the maximum strain is reached or the opening angle reaches 90°. The force-displacement curve is plotted after as well.

2.3.2 Discussion

Kirigami skins with the defined pattern were tested under uniaxial tension. Figure 2.10 displays uniaxial tension results with the corresponding output from the computational model. Overall, the model is able to adequately predict tensile response, especially in samples with smaller hinges. The model under predicts the amount of force on the elements experience at almost every strain. A major reason for discrepancies between the two data sets is due to the amount of uncertainty that is present during tensile testing. It is almost impossible to create a perfectly connected skin, which causes the forces on each element to be slightly different. In turn, the elements do not all simultaneously snap from in-plane rotation to out-of-plane deformation. There is a period in which individual elements will randomly snap into the out-of-plane position, creating a smoother transition into the second deformation cycle. In addition, the end condition in which the skin has kirigami elements connected to the uncut material affect the system. These boundary elements are not able to become fully expressed as the elements in the center of the skin causing the forces through them to be uneven. Overall, for the initial attempt to mathematically replicate the deformation of the kirigami skins, the model does well.

Kirigami skins are implemented on soft actuators as a method for transforming internal pressurization into linear motion. The stroke curves show the internal pressure verses displacement are compared to model predictions in figure 2.10, and there is some similarity between the two sets. The model does not predict the actuation performance as well as the prediction for tensile performance due to greater uncertainty generated in the setup of the actuators. Even though the skin experiences almost identical deformation pattern when on the actuator, the stroke pattern does not present as such. In the second phase of expansion via out-of-plane buckling a the hinges presents as nearly linear while on the actuator and the model does not account for these differences.

There are other factors not accounted for in such a simple model. Primarily, the model assumes the skin is composed of rigid squares, when during deformation, some bending or stretching does occur in each element. The model neglects the friction between the inflatable and the skin which opposes the growth during pressurization. In addition, the inflatable may not be consistent for every trial as the latex can inflate randomly. Also, the connection of the skin with itself is not always perfect causing imperfect end conditions.

Overall, the model is able to predict the the deformation pattern of a kirigami skin with some
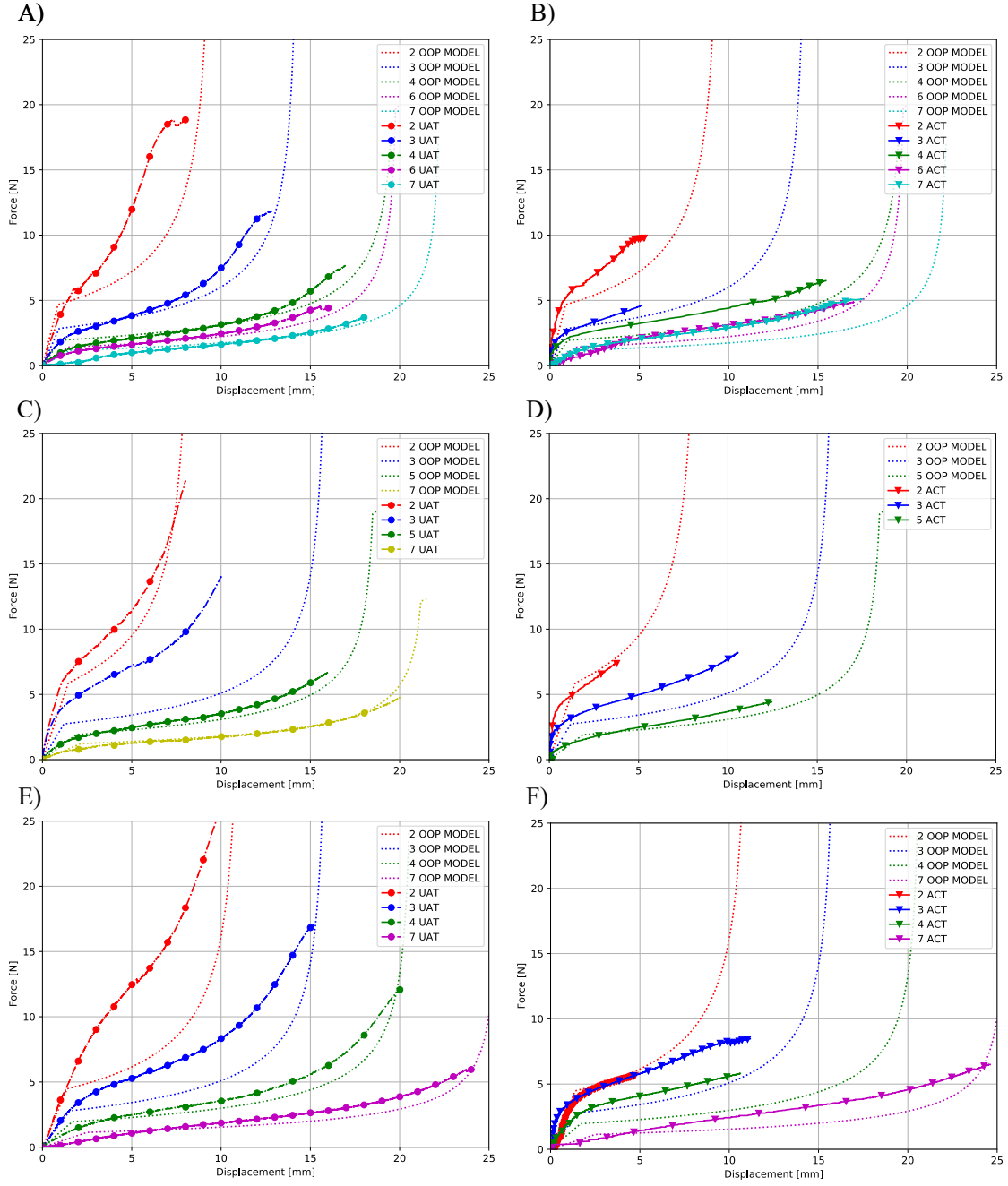
Figure 2.10: The force-displacement curves of the computation model compared with A,C,E) tensile testing results and B,D,F) actuation performance data. Each row represents samples with the same number of elements N.

accuracy. The mathematical equations that were purely theoretical were able to be implemented in order to predict experimental results. In the future, the goal would be to have a model that can output kirigami skin dimensions based on a desired actuation pattern.

Chapter 3

Auxetic Rectangular Kirigami

3.1 Design

W = 5   W = 3   W = 1

N = 8
R = 5

L_ℓ

L_C
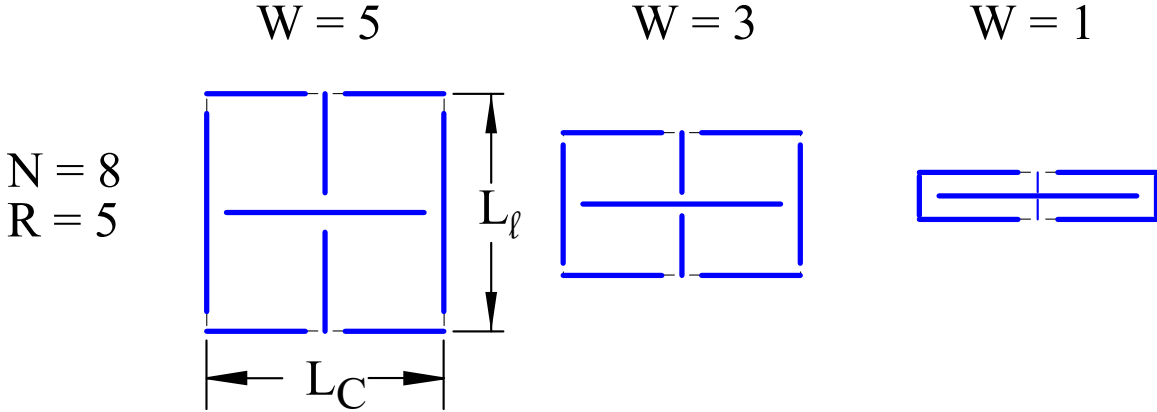
Figure 3.1: The design of a single element that includes the aspect ratio. The three designs have the same parameters for element size and cut ratio, N and R.

In addition to the parameters discussed previously, a third parameter was implemented into the kirigami pattern with the goal of increasing the stroke of the actuator. In all previously discussed samples, the individual rotating element was square. The *aspect ratio*, W, is set by equation 3.1 where L_l is the length of the element on the longitudinal axis (i.e. length wise) while L_C is the length of the element circumferentially. Figure 3.1 displays examples of an individual element with three different aspects, while all other parameters are kept constant. When $W = 5$ the element is
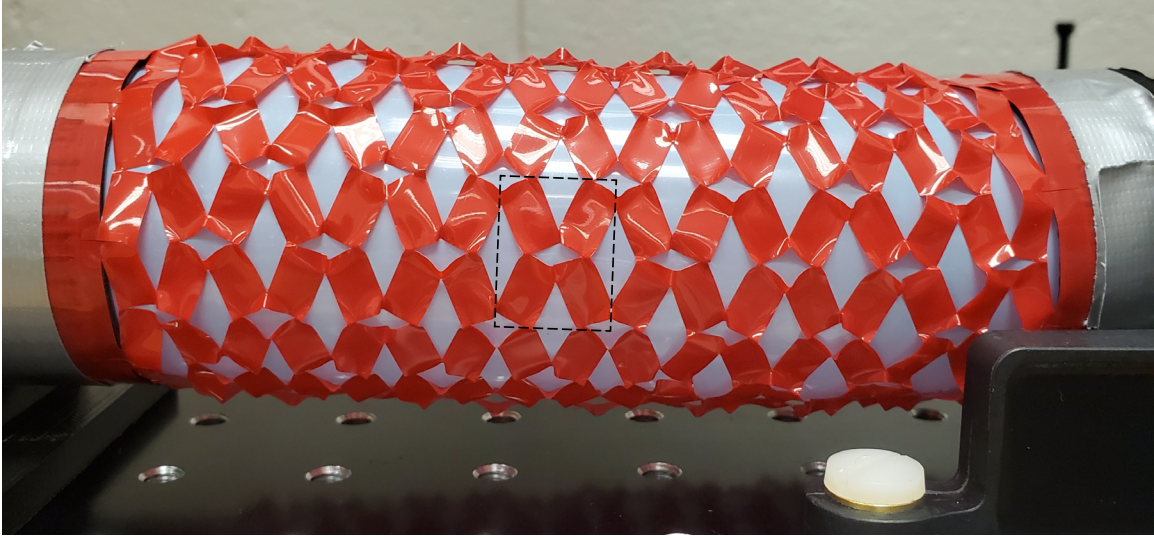
Figure 3.2: Example of the *rectangular* kirigami patterned skin while in use on a soft actuator. A individual element is denoted by the black dashed lines.

square and then becomes skinnier as the aspect ratio decreases.

$$\frac{L_l}{L_C} = \frac{W}{5} \tag{3.1}$$

Non-square elements present an advantage over square elements due to having increased displacement at the same opening angles. In addition to added strain through rotation, the actuators have increased stroke due to the ability to cut more elements longitudinally than before, essentially adding more links to a chain.

Through the data presented below, we show that altering the aspect ratio has the ability to increase the displacement of an actuator when compared to the square version of the same pattern. In addition, it does not require significantly more internal pressure to create the increase in displacement. Some issues arise in samples with *thin* elements, $W = 1, 2$, where the increase in strain is inversely related to the 'stability' of the sample due to the deformation pattern.

3.2 Results

Kirigami samples of varying aspect ratio, cut ratio, and number of elements were used as skins in actuation testing. The procedure follows the steps outlined originally; where the sample was

Figure 3.3: The actuator performance during extension. Each line is the linear regression of the the extension of one sample over multiple trials. The mean squared error is presented as shaded area above and below the fitted line.
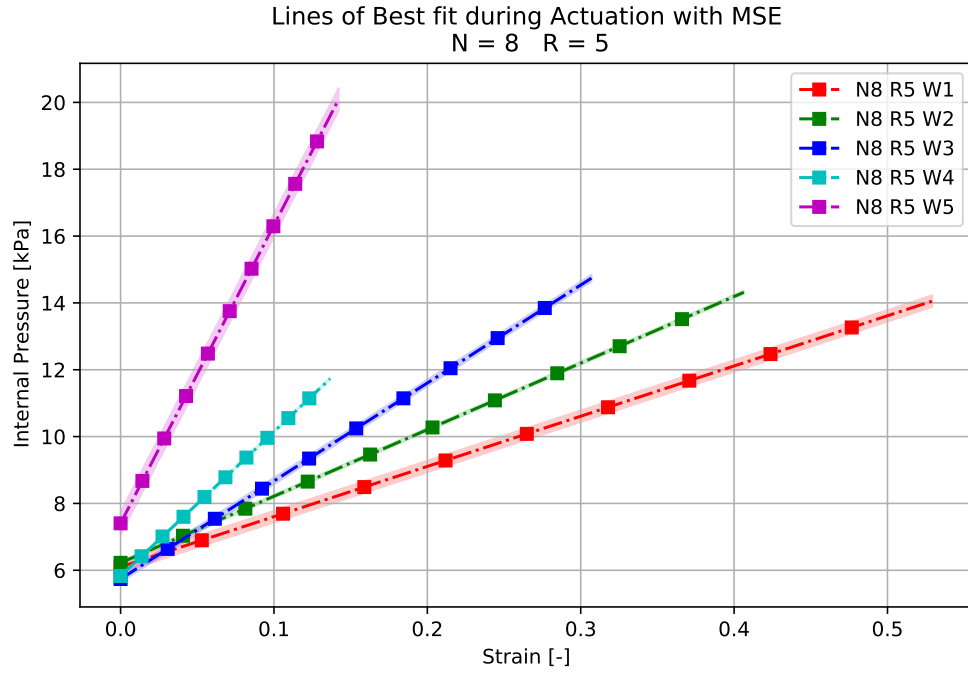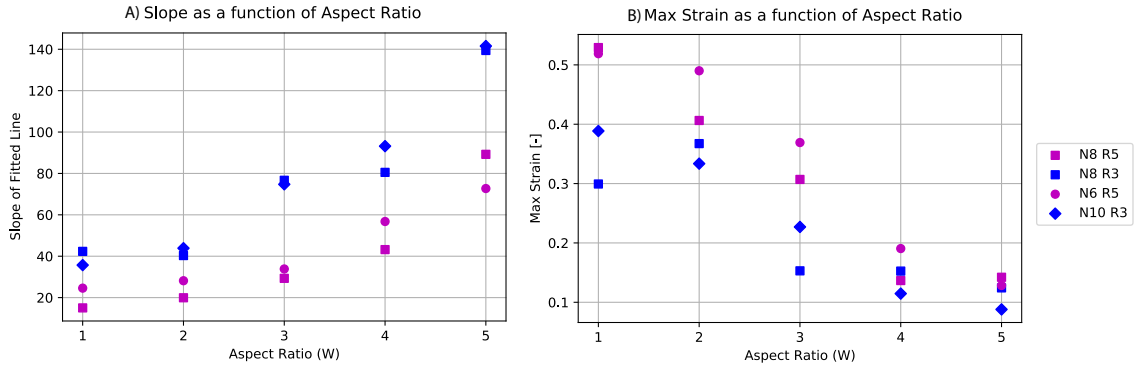

Figure 3.4: A) The slope of the linear regressions of the samples at each aspect ratio. B) the maximum strain of the samples as a function of the aspect ratio.

displaced to its maximum strain on the first cycle to plastically deform hinges, then on subsequent cycles was extended to close to the maximum strain. The subsequent trials follow almost identical extension curves, and linear regression analysis was performed to quantify the performance of the actuators. As the phase of linear growth occurs during the out-of-plane deformation, a dead pressure value was used as a cutoff in order to remove stroke data from during the first deformation phase. The line of best fits for samples with $N = 8$ and $R = 5$ and carried aspect ratio are plotted in figure 3.3. The mean squared error for each line is presented as a shaded region around each line.

Shown in figure 3.4A, as the aspect ratio *grows*(i.e. rectangles become closer to square), the slope of the extension becomes steeper and the maximum strain decreases. The slope of the pressure-strain curves represents an actuators sensitivity to change in pressure. At the thinnest rectangular samples, there are two main factors that cause the differences in sensitivity. First, the displacement between a closed rectangular element and fully opened element ($\theta \approx 45°$) is greater the thinner the rectangle is. In addition, the number of elements that can be cut into the same 4 inches of cut space is greater for samples with smaller aspect ratio. These two factors combine to create much higher strokes in elements with thin rectangular elements as opposed to simple square elements.

The trends found from parameterization of the square element skins hold true as well. The samples with larger hinges (R = 3 in blue) tend to provide slightly stiffer skins in response to change when compared to thinner hinges (R = 5 in magenta). This increased 'stiffness' leads to a more sensitive skin (fig 3.4A) that doesn't extend as far (fig 3.4B). The skins with rectangular elements follow the general trend that more elements causes slightly higher pressures.
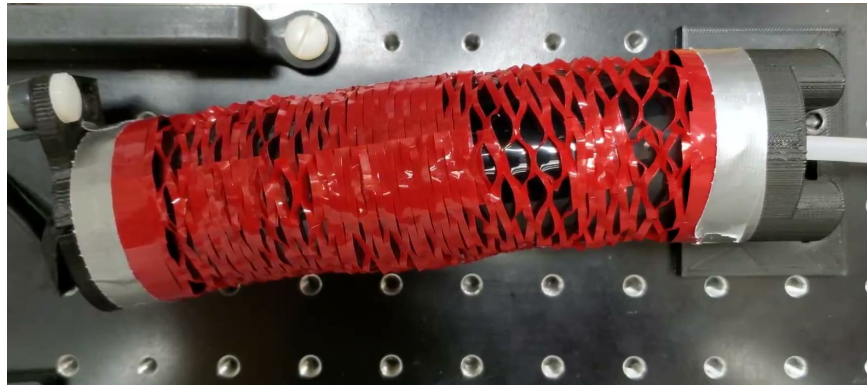
Figure 3.5: An actuator that has a kirigami skin with $W = 1$.

Although samples with thin elements ($W = 1, 2$) allow for large strains, the deformation pattern is unlike that of the more square elements. Figure 3.5 displays an example of a actuator with thin rectangular elements during pressurization. The pattern causes a loss in rigidity due to the mass amounts of cuts in the skin. When pressurized, the skin deforms not as a mesh of rotating rectangles, but as a linearly cut skin would deform. The cuts along the longitudinal axis are too small for rotation and out of plane deformation to occur. This causes a 'turning' of the skin to not be flat up against the surface of the inflatable, which produces instability. The lack of stability produces an actuator that is not able to extended linearly due to not being able to support its own weight.

Th addition of the aspect ratio parameter was successful in its implementation. By altering the aspect ratio, a wide range of stroke patterns were able to be achieved as rectangular elements increase the possible displacement of an actuator. This is further proof that kirigami skins can be effective means for tailoring the performance of a soft actuator to a specific task.

Chapter 4

Auxetic Parallelogram Kirigami

4.1 Design

In addition to linear motion of kirigami-wrapped actuators, we are proposing a new cutting pattern to induce a twisting motion during actuation. To create rotational motion, we created a skin that consisted of non-orthogonal elements as shown in figure 4.1. Each element is a equilateral parallelogram with overall side length of L, while all cuts, l_c, were cut on the y axis (the circumferential direction) or parallel to the offset angle. The parameters N and R affect the geometry of the cuts in the same manner as for orthogonal cut patterns. The overall goal is to produce an actuator that twists during linear extensions.

To test the twisting actuators, the previous procedure was not going to provide accurate linear or angular displacement data. Instead, the actuator was hung vertically with an analog pressure gauge that measured the internal pressure located beside it as shown in figure 4.2. A Samsung S10e recorded the actuation process and pressure gauge simultaneously . In order for data to be collected off the sample, green dots were added to the lower plastic cap to allow for proper tracking in post-processing. The inflation cycle of each specimen were recorded.

4.2 Results

The skins tested had the same parameters, $N = 8$ and $R = 5$, only differing in their offset angle. Samples were tested with an offset angle of 0°, 15°, 30°, 45°, and 60°. The videos
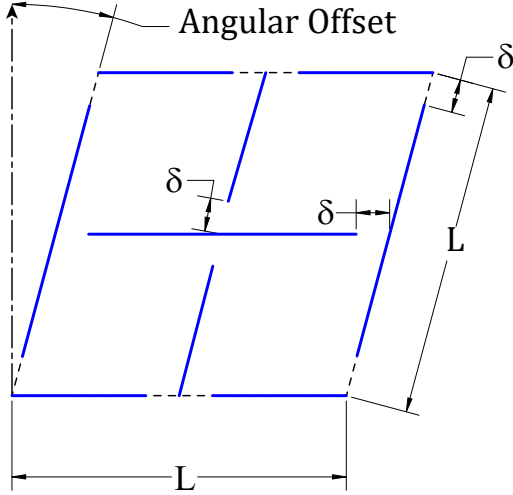
Figure 4.1: An example of an element with non-square angles. A parallelogram is presented, with all formerly vertical lines are now angular offset from the axis a set amount. The cuts in the sheet are represented by the blue markings.
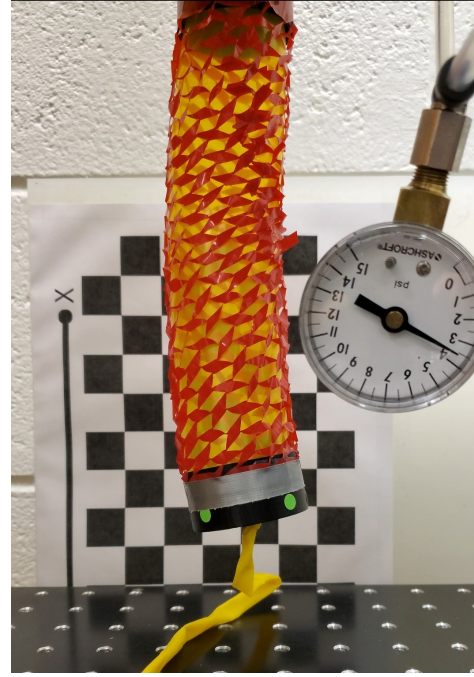
Figure 4.2: Experimental setup for recording both modes of deformation that occur during pressurization.

from each cycle were processed to obtain the angular and linear displacement of the end cap of the actuator. The pixel location of the end cap points was collected on a semi-continuous basis throughout inflation. Using a calibration image, the pixel locations were converted to millimeter displacements. The internal pressure was recorded frame by frame, with values linearly interpolated in-between as the inflation process is not always perfectly constant. In the end, figures 4.3 and 4.4 present the individual inflation cycles of the samples shown as colored lines. Linear regression was performed on the accumulation of cyclical data that occurred during the second deformation phase. Typically the R^2 values were above 0.9, meaning we can be confident in the consistency of the actuator performance.

When testing the sample with the larger offset angle, the displacements, both linear and angular, were more extreme. The larger the offset angle, the more sensitive the skin and actuator were to a change in pressure.

The deformation of the non-orthogonal skin follows similar phases as the orthogonally cut skins. To start, the internal angles are starting to open and all deformation is through in-plane rotation at the hinges. Then a critical point is reached and out of plane deformation begins. During

Figure 4.3: The A) angular and B) linear displacement of the actuator with the kirigami skin with angular offset of 60 degrees. The individual cycles are denoted by colored lines with a black line of best fit.
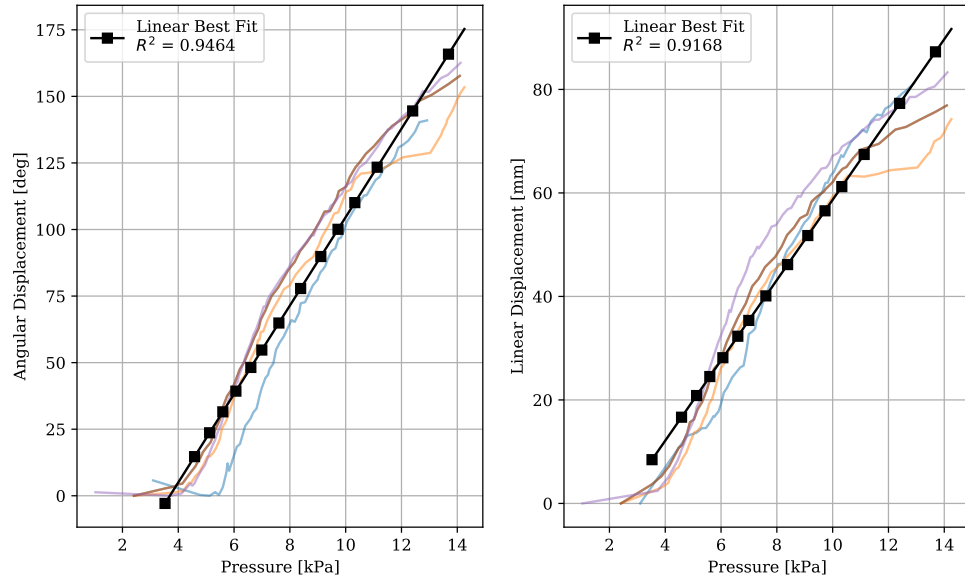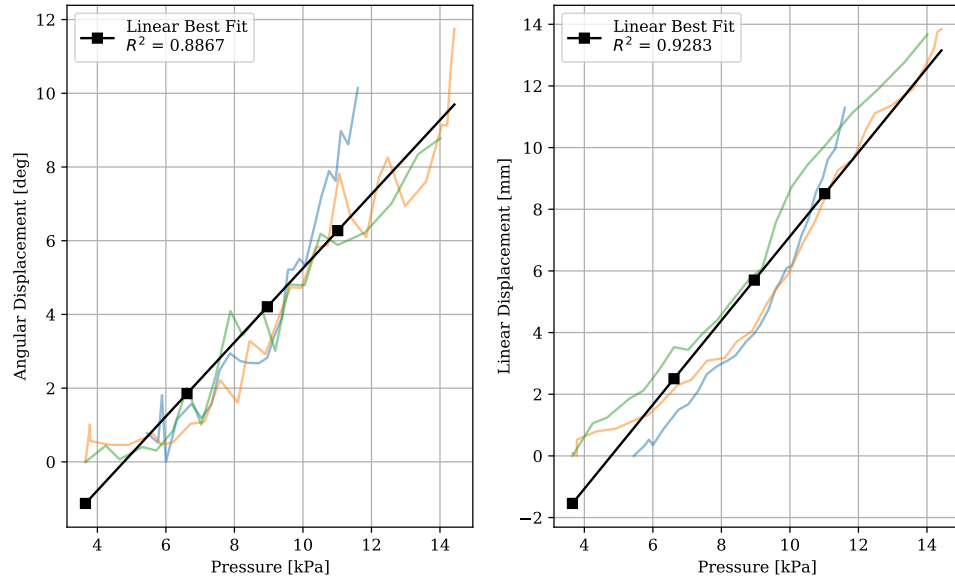
Figure 4.4: The A) angular and B) linear displacement of the actuator with the kirigami skin with angular offset of 15 degrees. The individual cycles are denoted by colored lines with a black line of best fit.

this second phase, twisting of the actuator starts as well. The addition of the offset angle causes a force and moment imbalance. The forces acting on the *sides* of the element have components in the longitudinal (x-direction in figure 4.1) and circumferential direction. As the strain is increased, the individual parallelograms open and displace opposite of the direction of the offset angle. The third phase of deformation was not present in samples with the smaller offset angle. But shown in figure 4.3, the sensitivity to change in pressure decreases at the end of the inflation cycle. This is evidence of a transition between deformation from a out of plane deformation to stretching through the hinges.

The results in figure 4.5 show that the larger the offset angle the greater the displacements. The exponential change that is seen between specimen is because of the change in offset angle and what that implies for the geometry of the individual element on each skin. A larger offset angle means larger unbalanced forces which lead to greater angular displacements. In addition, the offset angle creates "shorter" elements overall as the height of each is $h = L\sin(OA)$. For samples with offset angles of 45°and 60°, more elements are able to fit within the 4 in. available on the actuator creating for substantial linear and angular displacement.

Overall, the addition of the offset angle into the cutting pattern of the kirigami skins was successful in generating a twisting motion during actuation. The actuators were able to achieve significant twisting motion, almost completing a half-rotation. With further testing, coiling motion, twisting and bending simultaneously, may be achieved with the simple addition of a kirigami wrapper.
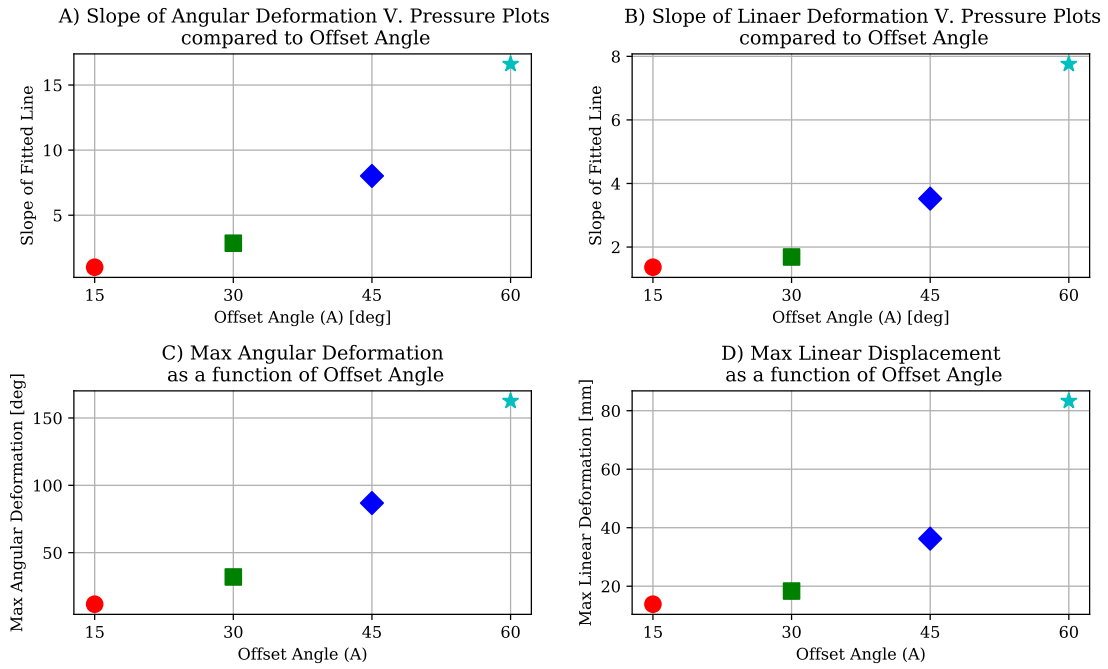
Figure 4.5: Comparing the actuation performance as function of offset angle by A) Slope of the linearly fitted angular deformation data B) Slope if the fitted linear deformation of each actuator C) The maximum angular deformation recorded during actuation D) The maximum linear displacement.

Chapter 5

Conclusion

We have shown that auxetic kirigami skins provide a unique nonlinear deformation process during uniaxial testing, which can be deconstructed into three-phases. Most deformation occurs once the hinges between elements have buckled out-of-plane. The same skins were then wrapped around soft pneumatic inflatables in the form of an actuator. During pressurization, the skins constrained the motion of the actuators to a distinct pressure-strain curve based on the skins' parameters. The cut ratio parameter (R) was shown to have a substantial effect the performance of the actuators, as the hinge size was inversely related to the maximum strain while requiring much less force to achieve that displacement. The number of elements (N) was shown to have some affect on the amount of pressure required to generate displacement. By altering two design parameters of the cutting geometry, a vast range of stroke patterns can be achieved.

During actuation, the skins undergo elastic and plastic deformation at the hinges. To achieve a consistent actuation process, the skins must be deformed to their maximum possible strain first, as stretching to a larger strain will cause plastic deformation in the hinges, altering the pressure required at a given strain. This process is essentially *breaking in* the skin before being used.

Even though designing and cutting a kirigami skin is relatively quick process, testing and quantifying the skin or actuator performance can be a time intensive process. A computation model was created to help simulate the force-displacement curves of the skin during tensile testing. The model was successful at estimating the deformation pattern, even with large assumptions.

In addition to the two original design parameters for the kirigami pattern, the aspect ratio parameter (W) was included into the design of an element. By altering the aspect ratio, the skin can

be an array of rectangular rotational elements. The rectangular elements were extremely successful at enabling actuators to generate significantly larger deformations than their square equivalents. Lastly, an angular offset parameter was introduced in an attempt to make an actuator that twists. The angular offset design variable creates a skin that is an array of rotating parallelograms. Preliminary testing showed that the greater the offset angle is the larger the angular and linear deformations of that actuator will be. The addition of two addition design variables into a simple cutting pattern were successful in widening the scope of possible actuation patterns.

Auxetic kirigami is a novel mechanical tool for it has a negative Poisson's ratio from simple cutting. Kirigami skins are a cheap tool that can be applied in numerous ways, and we have shown that they are effective when applied on soft actuators. Even though kirigami wrapped actuators still have present some uncertainty, the ability to rapidly design and manufacture new skins is noteworthy. Simple kirigami patterns offer versatility in motion by minimal changes in design. This work provides a framework for the design and construction of kirigami skins as a method for altering the displacement of linear soft pneumatic actuators.

5.0.1   Future Work

The work presented in this paper outlines the basic steps to creating a soft pneumatic actuator with kirigami skins. Further work can be directed at eliminating or lessening the uncertainty from the test to test. Applying the skins to the actuators is a delicate process that is done by hand, and creating a more exact system for getting a perfect connection along the overlapping column of elements will improve consistency. For example, if the overlapping column is not perfectly aligned the elements in it will not be able to open as predicted. In addition to altering the deformation of the actuator, it weakens the skin as the hinges experience higher forces to account for inconsistency.

In addition, the mathematical model can be expanded to include some of the finer impacts that act on the skin during deformation. The current model makes numerous assumptions to simplify the system. A finite element model could also be created to solve the same problem.

The next steps in continuing on with this research would be to expand on the possible actuation motions that can be generated by adding a kirigami skin. We have outlined in detail the steps for creating a skin for linear actuation, and we have shown how parallelogram kirigami provides twisting to linear deformation. Bending and coiling should be possible to achieve based on the same kirigami principles applied here.

The possible applications of auxetic kirigami are starting to be explored. If kirigami skins are to be applied in a work environment, the system would need to be updated to be more robust. The current actuators are fragile and fail easily if over pressurized. The kirigami skins are essentially sheets with cracks purposefully designed *cracks* in it. When over stressed, the skin tears at the thin hinges which ultimately leads to total failure of the skin. If the cuts were rounded at the ends near the hinges, the stress distribution will be friendlier to more higher forces. Also, an exploration into the material that is used for the kirigami should provide a sheet that can withstand some extreme forces and still work as desired. Again, we are experiencing the beginning in the shift towards soft robotics, and the possibilities, especially for kirigami, seem endless.

Appendices

Appendix A   Actuator Fabrication
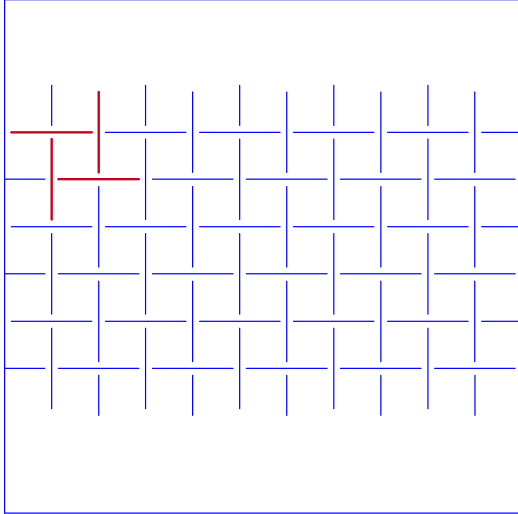
A.1   Skin Design

Figure 1: A small scale version of the orthogonal cut kirigami. The original four cuts are highlighted in red.

Figure 2: A sample kirigami skin directly after cutting. The overlapping column is covered in double sided tape.

To start, the kirigami pattern shown in the Design section is created in Solidworks. It was helpful to create a linear pattern of a four orthogonal cuts, highlighted in red in figure 1, that are spaced by the overall length of the element. Remember to include the extra column of elements on either the left or right side of the skin pattern. Once the pattern is completed in Solidworks, save the drawing as an Adobe Illustrator file (*.ai*).

In Illustrator, the internal cuts must be placed on a separate layer from the external outline cuts. This is vital as the internal pattern is initially cut into the sheet (Artus Corp.). After the first pass, a strip of double sided tape (Blick Industries) is aligned along one column of elements at either end of the sheet. The cutter now runs its second pass on the internal pattern, cutting through the tape, then in the final step, the entire skin is cut out. The final kirigami skin is shown in figure 2. The cuts into the double sided tape may need to be re-cut with an exacto knife as the paper cutter does not always cut completely through the thicker, taped areas.
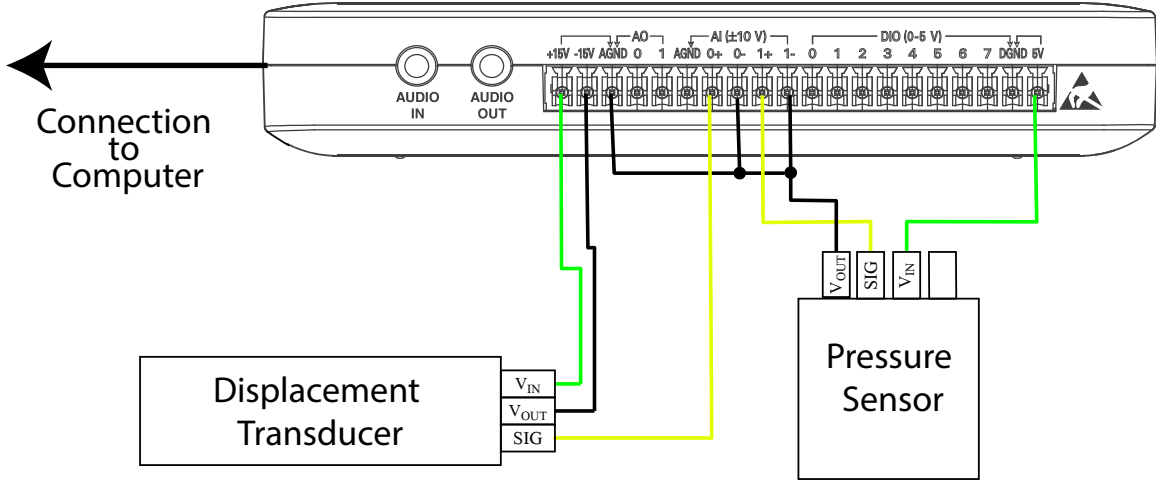
Figure 3: Electrical Wiring Schematic for Experimental Testing Hardware.

A.2   Experimental Setup

The next step for actuation testing is to get the actuator and experiment setup ready for the skin to be applied. First, seen in figure 3, the sensing technology is wired to a NI myDAQ (National Instruments). The displacement transducer is powered from the 15V source while the pressure sensor runs off of the 5V output. The signals from both sensors are wired into either 0+ or 1+ analog in terminals. The 0- and 1- terminals must be grounded to ensure consistent data. The myDAQ is then linked with a computer running LabView. Inside LabView, a program was written to collect data from both input streams simultaneously, which is then saved as a comma-separated values sheet (.csv). From here the data can be easily read by either Python or Matlab for further calibration and post processing.

The mounted end-cap is secured on the left side of the table, and the displacement transducer is placed 4 inches away. The magnetic target is attached to the free end cap. It is important to note that the displacement transducer measures the magnetic field so no magnetic materials can be located within a few inches of it during testing or results will not be accurate.

The pneumatic pressure is the next piece to be setup; the connections shown in figure 4. To start, connect all tubing to its proper location. It is pivotal to place a gate or lever valve before the junction which disperses the air to the sensors as the actuator needs to be cut-off from the supply pressure during actuation. The balloon (Qualatex Inc.) is tied to a undeformed length of about 1.5
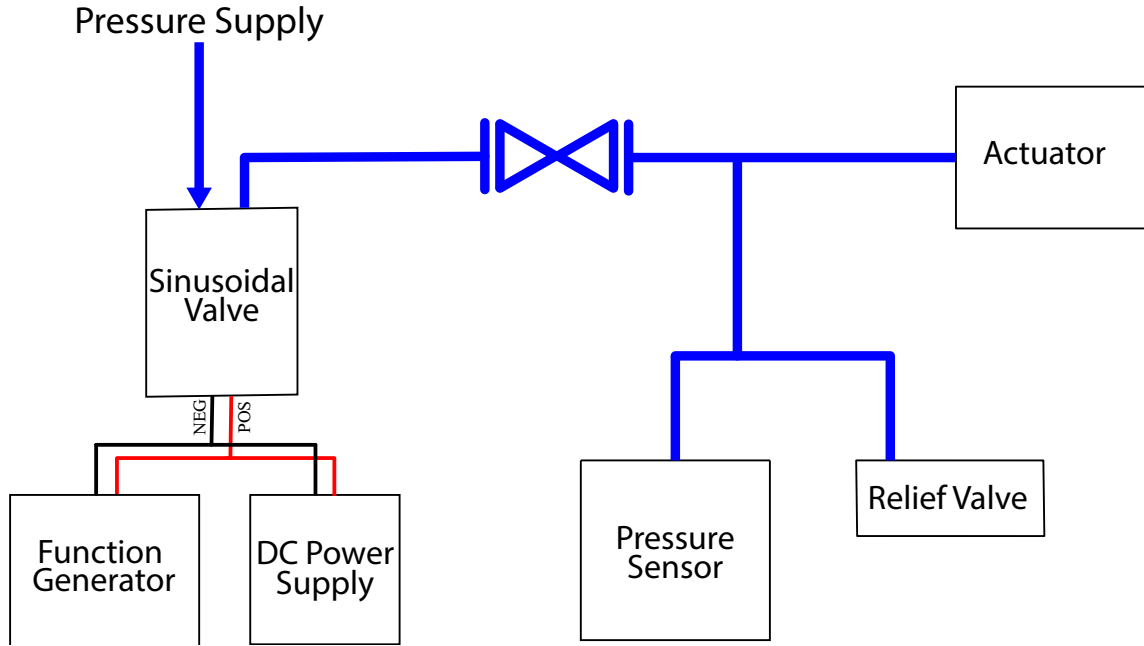
Figure 4: Pneumatic Schematic for experimental actuation testing.

to 2 inches long and is slipped through the opening in the mounted end-cap, while the knot from shortening is placed on the *outside* of the free end cap.

The function generator is set to output a flat DC signal to the sinusoidal valve. The DC power supply is configured to output 8 volts to the valve initially, and the power from the function generator is added to it. The two sources in combination actuate the valve to open and provide pneumatic pressure to the rest of the system. The user should only be altering the voltage output of the function generator, and it was found helpful to leave at 1.3 volts as this is enough pressure to *break* the balloon open.

Before the skin is applied to the actuator, the balloon is inflated to about 4 inches long. At this length, the skin should be easier to apply, and the sensors should be able to collect data.

A.3 Skin Application

Applying the skin to the actuator is a precise process as the quality of the connection of the skin to the actuator and the connection of the skin to itself is vital to performance of the actuator. First, small strips of double sided tape is applied around the outer circumference of each end cap to connect the skin and the caps. The side of the skin with the row of elements that have tape

over them is what is initially applied. It is important to get the overlapping edge as square to the end-caps as possible. The skin is then wrapped around the end-caps, ensuring there is a consistent connection between the caps and the skin.
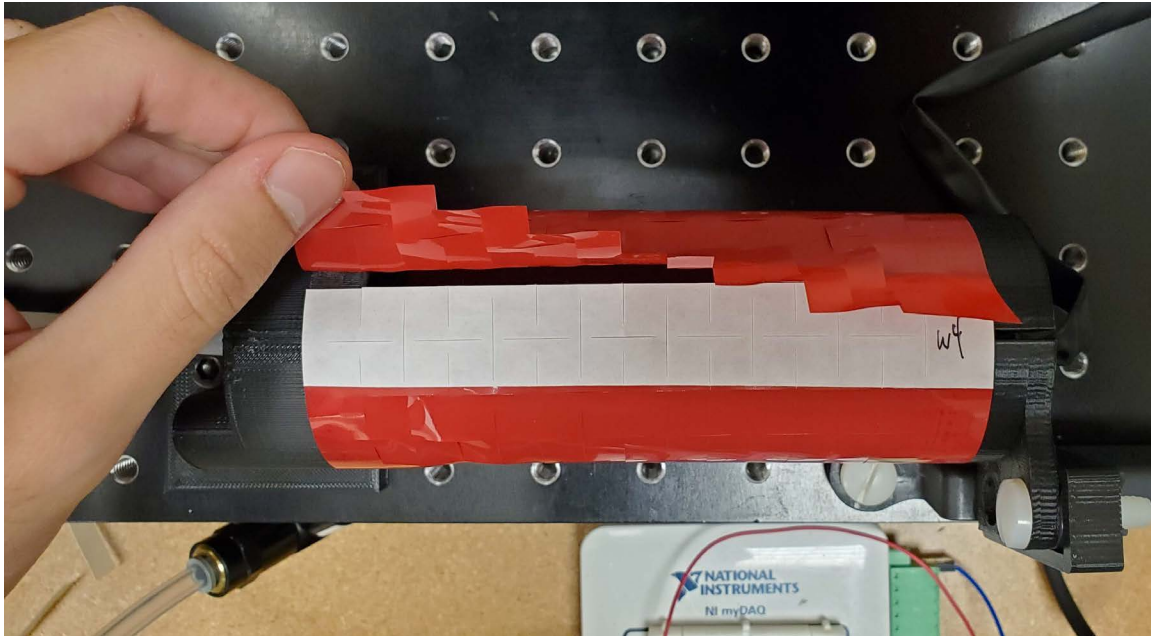
Figure 5: The skin during the wrapping process.

At this point the skin actuator and skin should look like figure 5. Then, with the adhesive layer of the double sided film showing, carefully place element on top of element. How well the two layers of elements are aligned affects the performance of the skin. To ensure the skin will not move during testing, a piece of vinyl or duct tape is placed over the uncut portions of the skin and the end-caps. Now, the user is ready for actuation testing and the actuator looks like figure 2.2.

Appendix B Computation Model Code

The following code is written in open-source Python 3.

```python
1  # -*- coding: utf-8 -*-
2  """
3  Created on Tue May 19 16:31:12 2020
4
5  @author: siannuc
6  """
7
8  # Out-of-Plane Buckling Model
9  # Assumes kirigami will buckle out of plane when the critical strain is reached
10 # See: Buckling Induced Kirigami (2015)
11
12 # INIT
13
14 import numpy as np
15 import pandas as pd
16 import math
17 import kiri_design_prop as kdp
18 import matplotlib.pyplot as plt
19
20 # FUNCTIONS
21
22 plt.rcParams["font.family"] = "serif"
23
24 global t, el,Ebar,delta, E, crit_strain, Nv, off
25
26 def Xftheta(theta_i):
27   # get X_i given a inplane opening angle
28   X = 2*el*(math.cos(theta_i)+math.sin(theta_i))
29   return X
30
31 def AngleFromStrain(eps):
32   # equation taken from Buckling Induced Kirigami(BIK)
33   y = eps + 1
34   phi = math.asin(y/(math.sqrt(2))) - math.pi/4
35   return phi # where phi is the angle from axis to element
36
37 def StrainEnergyI(ang):
38   # inplane strain energy - see BIK
39     U = (1/2)*Ebar*ang*ang
40     return U
41
42 def ForceFromStress(sigma):
43     F = 2*el*t*sigma*(1/1000)*(1/1000)
44     return F
45
46 def StrainOOP(theta):
47     # get OOP strain energy given an opening angle
48     U0 = (1/6)*E*((pow(delta,1)*pow(t,1))/(pow(el,2)))*theta
49     return U0
50
51 def betafunction(strain):
52     # get angle beta at a given strain
53     rhs = (off + strain)/(math.sqrt(2))
54     b = math.asin(rhs)-math.asin(off/math.sqrt(2))
55     return b
56
57 def alphafunction(strain, crit):
58     # get angle alpha at a given strain
59     b_x = betafunction(strain)
60     b_c = betafunction(crit+inc)
```

```python
61      rhs = .999-crit_strain - math.atan(b_x - b_c)
62      alpha = math.acos(math.sqrt(rhs))
63      alpha = math.acos(rhs)
64      return alpha
65
66 def theta_ofunction(strain, crit_strain):
67      # get OOP opening angle as a functino of strain
68      theta_o = math.atan(alphafunction(strain, crit_strain) + betafunction(strain))
69      theta_o = alphafunction(strain, crit_strain)**2 + betafunction(strain)**2
70      return theta_o
71
72 ## INPUTS
73
74 n = 5000 # number of iteration of loop
75
76 input_strain = 0.20 # max strain
77
78 t = 0.0508 # mm
79
80 # Design Parameters
81 N = 8
82 R = 3
83
84 global off
85 off = math.sqrt(2)-input_strain
86
87 L, cut_length, hinge_length = kdp.design_measure(N,R) # Get sizing of kirigami
        pattern - all in [mm]
88 # hinge_length is for (1) one hinge of the system.
89 delta = hinge_length
90
91 Nv = int(round(N/2)) # rough number of vertical elements
92
93 X_init = L
94 el = L/2
95 Ebar, crit_strain, E = kdp.Effective_YoungsMod(N, R) #[Pa], [-]
96
97 # initilize all needed for for loop and saving
98 strain_rain = np.linspace(0,input_strain, n) # get vector of strains
99 inc = strain_rain[1] # d*epsilon
100 force = np.zeros(n)
101 force_simp = np.zeros(n)
102 displacements = np.zeros(n)
103 norm_sig = np.zeros(n)
104 Ui = np.zeros(n)
105 Ub = np.zeros(n)
106 thetasi = np.zeros(n)
107 thetaso = np.zeros(n)
108 delUb = np.zeros(n)
109 delUi = np.zeros(n)
110 betas = np.zeros(n)
111 alphas = np.zeros(n)
112
113 i = 0
114 k = True
115 U_prev = 0
116
117 for eps in strain_rain:
118      # steps for both in-plane and out-of-plane model
119
120      displacements[i] = Nv*eps*X_init # X_i
121      # strain to angles
122
123      theta_i = AngleFromStrain(eps) # get opening angle for inplane
```

```python
124      U_i = StrainEnergyI(eps) # in-plane strain energy
125
126      theta_o = theta_ofunction(eps, crit_strain) # out of plane opening angle
127
128      thetasi[i] = theta_i
129      thetaso[i] = theta_o
130
131      alphas[i] = alphafunction(eps,crit_strain) # get alpha
132      betas[i] = betafunction(eps) # get beta
133
134      U_b = StrainOOP(theta_o) + StrainEnergyI(crit_strain) # find buckled strain
         energy
135
136      calc_crit = StrainEnergyI(crit_strain)
137
138      delUi[i] = U_i-Ui[i-1] # find change in in-plane energy
139      delUb[i] = U_b-Ub[i-1] # find change in OOP energy
140
141      sigmai = delUi[i]/inc
142      sigmao = delUb[i]/inc
143
144      if sigmai < sigmao:
145          # Still in First Region - buckling has not occured yet
146
147          sigma = sigmai
148
149          force[i] = ForceFromStress(sigma)
150          Ui[i] = U_i
151          Ub[i] = U_b
152
153          U_prev = U_i
154
155      else: # buckling has occured
156          if k == True:
157              crit_eps = eps
158              print('OOP Deformations')
159              k = False
160
161          sigma = sigmao
162
163          force[i] = ForceFromStress(sigma)
164          Ui[i] = U_i
165          Ub[i] = U_b
166
167          if i < 20:
168              print(i)
169              print(U_prev)
170              print(U_b)
171
172          U_prev = U_b
173      if theta_o > math.pi/2:
174          break
175
176      i += 1
177
178 #%% Plotting
179 plt.figure(figsize = (10,6))
180 title = 'N: ' + str(N) + ' - R: ' + str(R)
181 plt.plot(displacements[0:i], force[0:i], color = 'blue', ls = '-', label = 'Strain-
     Method')
182 plt.xlabel('Displacement [mm]')
183 plt.ylabel('Force [N]')
184 plt.title(title)
185 plt.grid(True)
```

```
186 plt.legend()
187 plt.show()
```
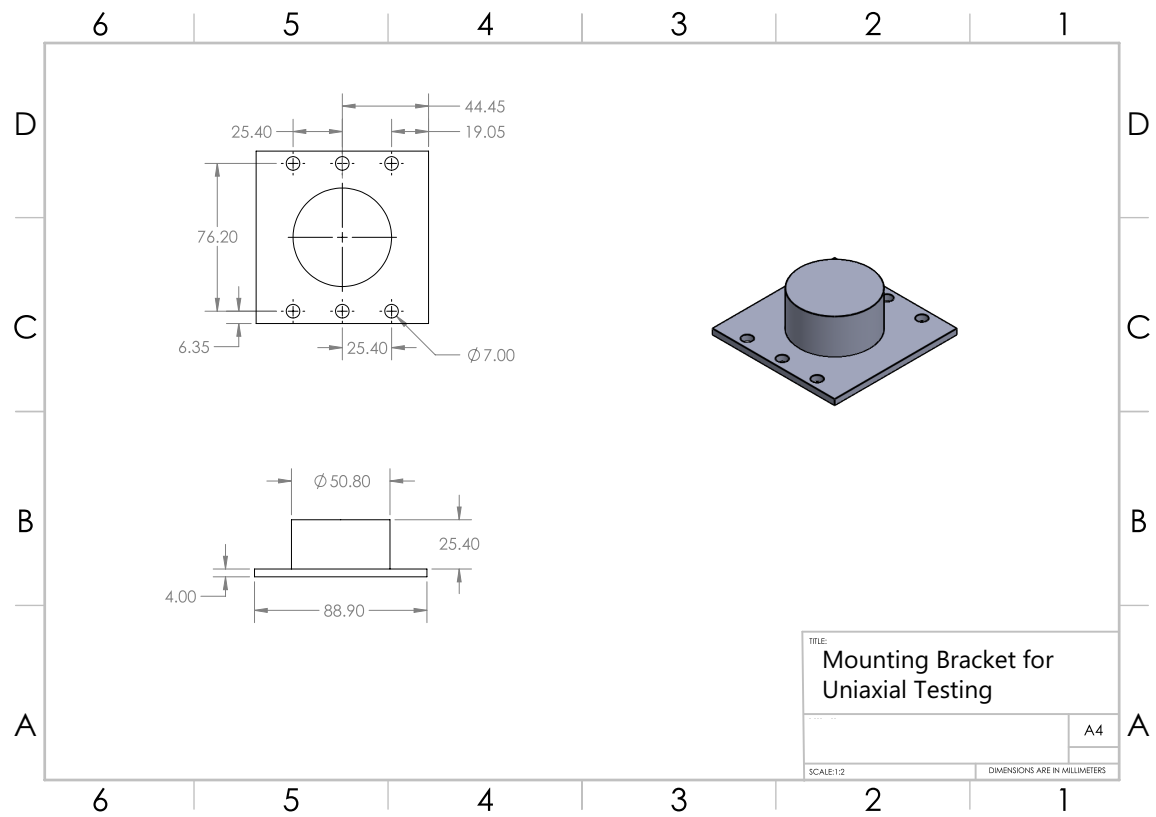
Appendix C   Drawings

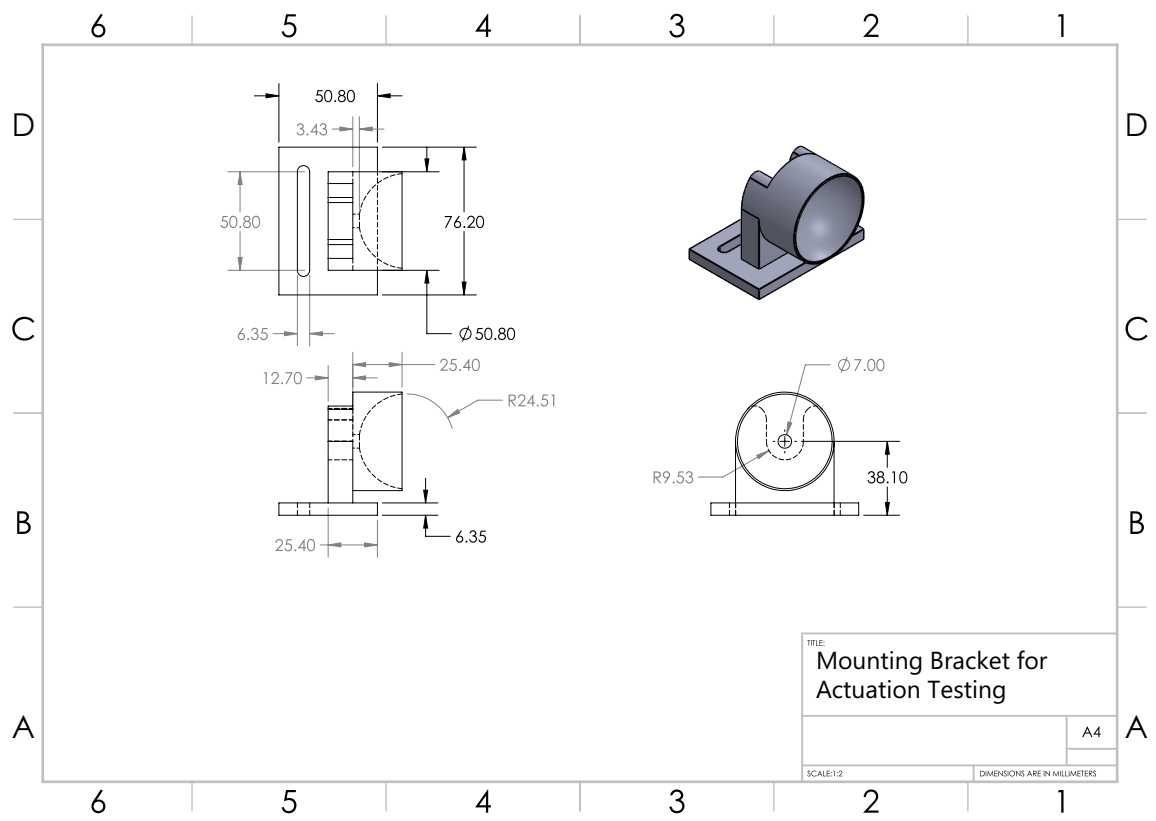Figure 6: Mounting unit for uniaxial tensile testing.
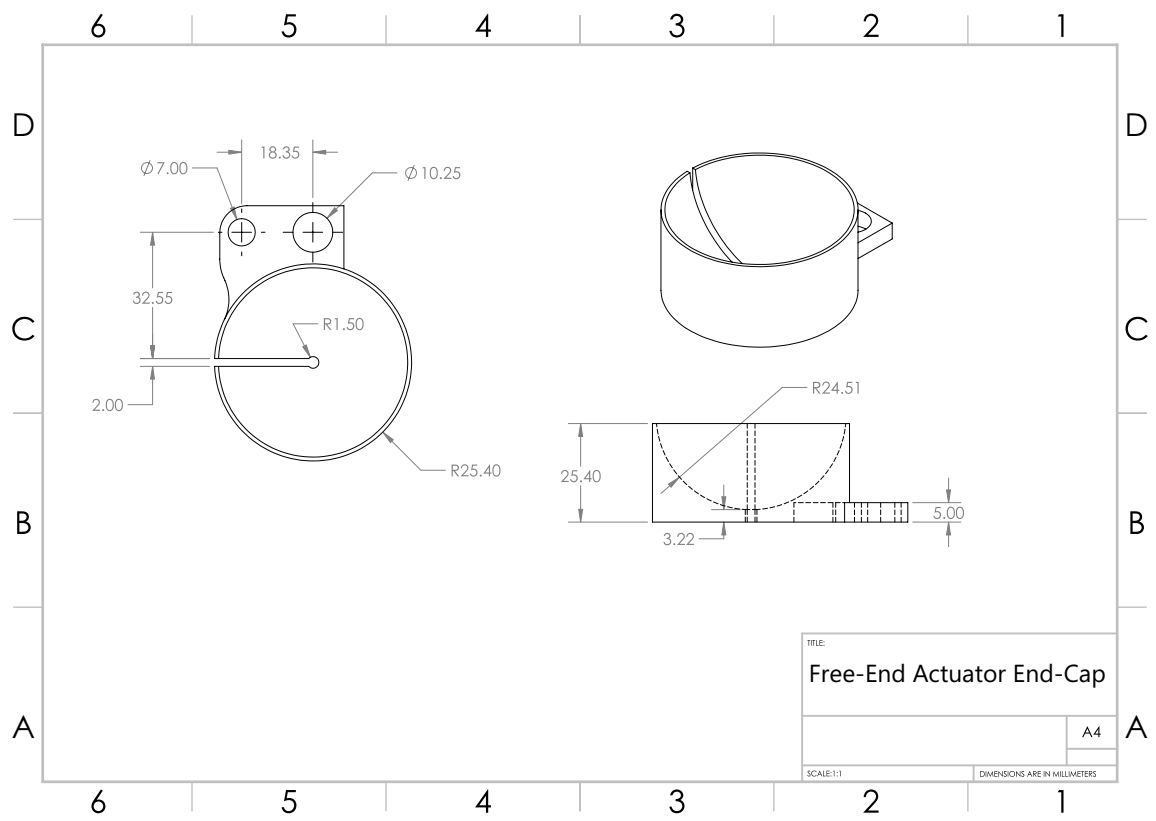
Figure 7: Mounted end-cap of soft actuator.

Figure 8: Free end-cap of soft actuator.

Bibliography

[1] F. Schmitt, O. Piccin, L. Barbé, and B. Bayle, "Soft Robots Manufacturing : A Review," vol. 5, no. July, 2018.

[2] C. Lee, M. Kim, Y. J. Kim, N. Hong, S. Ryu, H. J. Kim, and S. Kim, "Soft robot review," no. January, 2017.

[3] F. Ilievski, A. D. Mazzeo, R. F. Shepherd, X. Chen, and G. M. Whitesides, "Zuschriften Soft Robotics for Chemists **," pp. 1930–1935, 2011.

[4] M. Calisti, M. Giorelli, G. Levy, B. Mazzolai, B. Hochner, C. Laschi, and P. Dario, "An octopus-bioinspired solution to movement and manipulation for soft robots," *Bioinspiration and Biomimetics*, vol. 6, no. 3, 2011.

[5] S. Seok, N. Labs, C. D. Onal, and K.-j. Cho, "Meshworm : A Peristaltic Soft Robot With Antagonistic Nickel Titanium Coil Actuators," no. October, 2013.

[6] M. Shahinpoor, J. O. Simpson, and J. Smith, "Ionic polymer – metal composites (IPMCs) as biomimetic sensors , actuators and artificial muscles — a review," 1998.

[7] M. Shahinpoor, "Ionic polymer-conductor composites as biomimetic sensors, robotic actuators and artificial muscles - A review," *Electrochimica Acta*, vol. 48, no. 14-16 SPEC., pp. 2343–2353, 2003.

[8] A. Punning, M. Kruusmaa, and A. Aabloo, "Surface resistance experiments with IPMC sensors and actuators," *Sensors and Actuators, A: Physical*, vol. 133, no. 1, pp. 200–209, 2007.

[9] R. K. Katzschmann, A. D. Marchese, and D. Rus, "Hydraulic Autonomous Soft Robotic Fish for 3D Swimming," 2016.

[10] Y. Sun, Y. S. Song, and J. Paik, "Characterization of silicone rubber based soft pneumatic actuators," *IEEE International Conference on Intelligent Robots and Systems*, pp. 4446–4453, 2013.

[11] F. Ilievski, A. D. Mazzeo, R. F. Shepherd, X. Chen, and G. M. Whitesides, "Soft robotics for chemists," *Angewandte Chemie - International Edition*, vol. 50, no. 8, pp. 1890–1895, 2011.

[12] P. Polygerinos, S. Lyne, Z. Wang, L. Fernando, B. Mosadegh, G. M. Whitesides, and C. J. Walsh, "Towards a Soft Pneumatic Glove for Hand Rehabilitation," pp. 1512–1517, 2013.

[13] B. Mosadegh, P. Polygerinos, C. Keplinger, S. Wennstedt, R. F. Shepherd, U. Gupta, J. Shim, K. Bertoldi, C. J. Walsh, and G. M. Whitesides, "Pneumatic networks for soft robotics that actuate rapidly," *Advanced Functional Materials*, vol. 24, no. 15, pp. 2163–2170, 2014.

[14] R. F. Shepherd, F. Ilievski, W. Choi, S. A. Morin, A. A. Stokes, A. D. Mazzeo, X. Chen, M. Wang, and G. M. Whitesides, "Multigait soft robot," pp. 1–4, 2011.

[15] M. T. Tolley, R. F. Shepherd, B. Mosadegh, K. C. Galloway, M. Wehner, M. Karpelson, R. J. Wood, and G. M. Whitesides, "A Resilient, Untethered Soft Robot," *Soft Robotics*, vol. 1, no. 3, pp. 213–223, 2014.

[16] C. P. Chou and B. Hannaford, "Measurement and modeling of McKibben pneumatic artificial muscles," *IEEE Transactions on Robotics and Automation*, vol. 12, no. 1, pp. 90–102, 1996.

[17] B. Tondu and P. Lopez, "Artificial Muscle Robot Actuators," *Control Systems,IEEE*, vol. 20, no. 2, pp. 15–38, 2000.

[18] F. Connolly, P. Polygerinos, C. J. Walsh, and K. Bertoldi, "Mechanical programming of soft actuators by varying fiber angle," *Soft Robotics*, vol. 2, no. 1, pp. 26–32, 2015.

[19] K. C. Galloway, P. Polygerinos, C. J. Walsh, and R. J. Wood, "Mechanically Programmable Bend Radius for Fiber-Reinforced Soft Actuators," 2013.

[20] P. Maeder-york, T. Clites, E. Boggs, R. Neff, P. Polygerinos, L. Stirling, and K. Galloway, "Biologically Inspired Soft Robot for Thumb Rehabilitation,"

[21] T. Wang, Y. Zhang, Y. Zhu, and S. Zhu, "A computationally efficient dynamical model of fluidic soft actuators and its experimental verification," *Mechatronics*, vol. 58, no. October 2018, pp. 1–8, 2019.

[22] R. Geer, S. Iannucci, and S. Li, "Pneumatic Coiling Actuator Inspired by the Awns of Erodium cicutarium," *Frontiers in Robotics and AI*, vol. 7, 2020.

[23] F. Connolly, C. J. Walsh, and K. Bertoldi, "Automatic design of fiber-reinforced soft actuators for trajectory matching," *Proceedings of the National Academy of Sciences of the United States of America*, vol. 114, no. 1, pp. 51–56, 2017.

[24] S. Satheeshbabu and G. Krishnan, "Designing systems of fiber reinforced pneumatic actuators using a pseudo-rigid body model," *IEEE International Conference on Intelligent Robots and Systems*, vol. 2017-Septe, pp. 1201–1206, 2017.

[25] R. Deimel and O. Brock, "A Novel Type of Compliant, Underactuated Robotic Hand for Dexterous Grasping," 2015.

[26] Y. Zhang, Z. Yan, K. Nan, D. Xiao, Y. Liu, H. Luan, H. Fu, X. Wang, Q. Yang, J. Wang, W. Ren, H. Si, F. Liu, L. Yang, H. Li, J. Wang, X. Guo, H. Luo, L. Wang, Y. Huang, and J. A. Rogers, "A mechanically driven form of Kirigami as a route to 3D mesostructures in micro/nanomembranes," *Proceedings of the National Academy of Sciences of the United States of America*, vol. 112, no. 38, pp. 11757–11764, 2015.

[27] A. Lamoureux, K. Lee, M. Shlian, S. R. Forrest, and M. Shtein, "Dynamic kirigami structures for integrated solar tracking," *Nature Communications*, pp. 1–6, 2015.

[28] Y. C. Cheng, H. C. Lu, X. Lee, H. Zeng, and A. Priimagi, "Kirigami-Based Light-Induced Shape-Morphing and Locomotion," *Advanced Materials*, vol. 32, no. 7, 2020.

[29] K. Cai, J. Luo, Y. Ling, J. Wan, and Q. H. Qin, "Effects of size and surface on the auxetic behaviour of monolayer graphene kirigami," *Scientific Reports*, 2016.

[30] M. K. Blees, A. W. Barnard, P. A. Rose, S. P. Roberts, K. L. McGill, P. Y. Huang, A. R. Ruyack, J. W. Kevek, B. Kobrin, D. A. Muller, and P. L. McEuen, "Graphene kirigami," *Nature*, vol. 524, no. 7564, pp. 204–207, 2015.

[31] J. N. Grima, S. Winczewski, L. Mizzi, M. C. Grech, R. Cauchi, R. Gatt, D. Attard, K. W. Wojciechowski, and J. Rybicki, "Tailoring graphene to achieve negative poisson's ratio properties," *Advanced Materials*, vol. 27, pp. 1455–1459, 2 2015.

[32] N. Wei, Y. Chen, K. Cai, J. Zhao, H.-q. Wang, and J.-c. Zheng, "Thermal conductivity of graphene kirigami : Ultralow and strain robustness," *Carbon*, vol. 104, pp. 203–213, 2016.

[33] A. Firouzeh, T. Higashisaka, K. Nagato, K. Cho, and J. Paik, "Stretchable kirigami components for composite meso-scale robots," *IEEE Robotics and Automation Letters*, vol. 5, no. 2, pp. 1883–1890, 2020.

[34] J. Cui, F. R. Poblete, and Y. Zhu, "Origami/Kirigami-Guided Morphing of Composite Sheets," *Advanced Functional Materials*, vol. 28, no. 44, pp. 1–7, 2018.

[35] A. Lele, V. Deshpande, O. Myers, and S. Li, "Snap-through and stiffness adaptation of a multistable Kirigami composite module," *Composites Science and Technology*, vol. 182, no. July, p. 107750, 2019.

[36] A. Rafsanjani, A. Akbarzadeh, and D. Pasini, "Snapping Mechanical Metamaterials under Tension," *Advanced Materials*, vol. 27, no. 39, pp. 5931–5935, 2015.

[37] B. Liu, Y. Ozkan-aydin, D. I. Goldman, and F. L. H. Iii, "Kirigami Skin Improves Soft Earthworm Robot Anchoring and Locomotion Under Cohesive Soil," 2019.

[38] C. Branyan, R. L. Hatton, and Y. Menguc, "Snake-inspired kirigami skin for lateral undulation of a soft snake robot," *IEEE Robotics and Automation Letters*, vol. 5, no. 2, pp. 1728–1733, 2020.

[39] J. N. Grima and K. E. Evans, "Auxetic behavior from rotating squares," *Journal of Materials Science Letters*, vol. 19, no. 17, pp. 1563–1565, 2000.

[40] J. N. Grima, V. Zammit, R. Gatt, A. Alderson, and K. E. Evans, "Auxetic behaviour from rotating rigid units," *Physica Status Solidi (B) Basic Research*, vol. 244, no. 3, pp. 866–882, 2007.

[41] J. N. Grima, E. Manicaro, and D. Attard, "Auxetic behaviour from connected different-sized squares and rectangles," *Proceedings of the Royal Society A: Mathematical, Physical and Engineering Sciences*, vol. 467, no. 2126, pp. 439–458, 2011.

[42] A. Rafsanjani and K. Bertoldi, "Buckling-Induced Kirigami," *Physical Review Letters*, vol. 118, 2 2017.

[43] A. Rafsanjani, L. Jin, B. Deng, and K. Bertoldi, "Propagation of pop ups in kirigami shells," *Proceedings of the National Academy of Sciences of the United States of America*, vol. 116, no. 17, pp. 8200–8205, 2019.